AGU PUBLICATIONS

JGR

Journal of Geophysical Research: Atmospheres

RESEARCH ARTICLE
10.1002/2016JD025303

Key Points:
- Characterization of vertical velocity, area fraction, and mass flux profiles for Amazon convection
- Profiles aligned to be statistically representative of ensemble and aggregate convective properties to GCM domain scales
- Convective profiles indicate significant sensitivity to environmental forcing, wet and dry season regime controls

Correspondence to:
S. E. Giangrande,
sgrande@bnl.gov

Citation:
Giangrande, S. E., T. Toto, M. P. Jensen, M. J. Bartholomew, Z. Feng, A. Protat, C. R. Williams, C. Schumacher, and L. Machado (2016), Convective cloud vertical velocity and mass-flux characteristics from radar wind profiler observations during GoAmazon2014/5, *J. Geophys. Res. Atmos.*, *121*, 12,891–12,913, doi:10.1002/2016JD025303.

Received 2 MAY 2016
Accepted 20 OCT 2016
Accepted article online 21 OCT 2016
Published online 15 NOV 2016
Corrected 24 MAY 2019

This article was corrected on 24 MAY 2019. See the end of the full text for details. All corrections have been made to the online version.

Convective cloud vertical velocity and mass-flux characteristics from radar wind profiler observations during GoAmazon2014/5

Scott E. Giangrande[1], Tami Toto[1], Michael P. Jensen[1], Mary Jane Bartholomew[1], Zhe Feng[2], Alain Protat[3], Christopher R. Williams[4], Courtney Schumacher[5], and Luiz Machado[6]

[1]Environmental and Climate Sciences Department, Brookhaven National Laboratory, Upton, New York, USA, [2]Pacific Northwest National Laboratory, Richland, Washington, USA, [3]Centre for Australian Weather and Climate Research, Melbourne, Victoria, Australia, [4]University of Colorado Boulder and NOAA/Earth System Research Laboratory/Physical Sciences Division, Boulder, Colorado, USA, [5]Texas A&M University, College Station, Texas, USA, [6]National Institute for Space Research, Sao Jose dos Campos, Brazil

Abstract A radar wind profiler data set collected during the 2 year Department of Energy Atmospheric Radiation Measurement Observations and Modeling of the Green Ocean Amazon (GoAmazon2014/5) campaign is used to estimate convective cloud vertical velocity, area fraction, and mass flux profiles. Vertical velocity observations are presented using cumulative frequency histograms and weighted mean profiles to provide insights in a manner suitable for global climate model scale comparisons (spatial domains from 20 km to 60 km). Convective profile sensitivity to changes in environmental conditions and seasonal regime controls is also considered. Aggregate and ensemble average vertical velocity, convective area fraction, and mass flux profiles, as well as magnitudes and relative profile behaviors, are found consistent with previous studies. Updrafts and downdrafts increase in magnitude with height to midlevels (6 to 10 km), with updraft area also increasing with height. Updraft mass flux profiles similarly increase with height, showing a peak in magnitude near 8 km. Downdrafts are observed to be most frequent below the freezing level, with downdraft area monotonically decreasing with height. Updraft and downdraft profile behaviors are further stratified according to environmental controls. These results indicate stronger vertical velocity profile behaviors under higher convective available potential energy and lower low-level moisture conditions. Sharp contrasts in convective area fraction and mass flux profiles are most pronounced when retrievals are segregated according to Amazonian wet and dry season conditions. During this deployment, wet season regimes favored higher domain mass flux profiles, attributed to more frequent convection that offsets weaker average convective cell vertical velocities.

1. Introduction

Understanding deep convective clouds and simulating their impacts is a major challenge from cloud resolving model (CRM) to global climate model (GCM) scales. At the GCM scales, convective parameterizations impact the simulation of the global energy balance and cumulus cloud radiative properties while also influencing the strength of the larger-scale atmospheric circulations that these models explicitly resolve [*Del Genio* 2012]. Therefore, an inability to adequately represent the lifecycle and impacts of deep convective clouds is a primary driver for GCM uncertainty in the prediction of climate change. For the foreseeable future, model reliance on convective parameterization schemes motivates many observational studies that explore new technologies to improve our insights into cloud processes and cloud-aerosol interactions [e.g., *May et al*., 2008; *Jakob*, 2010; *Jensen et al*., 2016; *Wang et al*., 2016]. Better understanding of deep convective lifecycle within undersampled tropical convective regions is often emphasized, since convective parameterization feedbacks over tropical regions have illustrated significant and far-reaching sensitivity for GCM predictive capabilities [e.g., *Yin et al*., 2013; *Hagos et al*., 2016].

There is demand for newer observational constraints to better isolate the connections between deep cloud humidity, entrainment, and microphysical treatments [e.g., *Milbrandt and Yau*, 2005; *Jensen and Del Genio*, 2006; *Del Genio et al*., 2012]. However, since deep convective clouds operate over a wide range of scales, it is difficult for any single observational platform to inform on convective lifecycle from detailed microphysical process scales to larger-scale cloud cover and energetic implications. Practical limitations have sparked

emphasis on multisensor, multiscale "supersite" activities to better bridge the gaps between cloud process studies and larger-scale feedbacks [e.g., *Stokes and Schwartz*, 1994; *Mather and Voyles*, 2013]. One notable recommendation has been to improve the observations of convective vertical velocity and mass flux over larger domains, necessary to evaluate traditional mass flux-driven ensemble GCM parameterization [e.g., *Arakawa and Schubert*, 1974]. These observations are also useful in the development of current and future GCM parameterizations that better differentiate organized convection lifecycle through additional cumulus complexity [e.g., *Donner et al*., 2001; *Storer et al*., 2015].

Traditionally, vertical velocity and mass flux estimates within deeper convection have been collected using narrow, high-resolution measurements obtained directly by aircraft [e.g., *Byers and Braham*, 1948; *Lenschow*, 1976; *LeMone and Zipser*, 1980; *Anderson et al*., 2005]. Although aircraft studies provide reliable measurements, the cost and practical hazards for flight operations in deeper convective cells limit the availability of these data sets. Recently, radar wind profilers (RWP) have emerged as a less expensive and safer alternative to aircraft studies [e.g., *Battan and Theiss*, 1970; *May and Rajopadhyaya*, 1999; *Williams*, 2012; *Giangrande et al*., 2013; *Schumacher et al*., 2015; *Kumjian et al*., 2016]. Recent profiler upgrades have enabled the collection of vertical velocity measurements at sufficient temporal and vertical resolution for convective core studies. These profiler retrievals report retrieval uncertainty to within 1–2 m s^{-1} [e.g., *Heymsfield et al*., 2010]. Nevertheless, fixed soda-straw wind profilers do not target convective cells (as might a directed aircraft field campaign) and lack the spatial domain sampling of scanning weather radar to conveniently align with CRM or GCM model outputs.

To make an appropriate use of RWPs for GCM evaluation, a key question is "To what extent are the estimated time mean properties (that wind profilers routinely collect) representative of area mean quantities (i.e., those of interest to the GCM community)?" GCM outputs represent ensemble cloud properties occupying large spatiotemporal domains (i.e., equal or greater than 1 h in time, 20 km horizontally). For practical considerations, previous studies have found it simpler to report the statistical, aggregated properties from subsets of easily identifiable convective "cores," e.g., those cores having stronger coherent updraft or downdraft signatures [e.g., *LeMone and Zipser*, 1980; *Zipser and LeMone*, 1980]. These efforts are complementary, since the statistics from a population of cores is still of interest to larger-scale models [e.g., *Donner*, 1993]. However, relying exclusively on these methods may fall short for conventional GCM-type mass flux definitions and evaluation that aggregate all convective cloud air motions to within a particular spatiotemporal domain.

Recently, *Kumar et al*. [2015] proposed a statistical RWP-based solution aimed at retrieving mass flux profiles around Darwin, Australia, better aligned for evaluating ensemble GCM simulations. The efforts broke from traditional aircraft or profiler core definitions, instead requiring a long profiler data set with surveillance radar support to ensure statistical alignment between point profiler and scanning radar domain sampling. Our study follows similar motivations to *Kumar et al*. [2015], using an extended profiler data set to build on our knowledge of deep convective vertical velocity and mass flux properties. As in that study, we document the vertical structure of convective mass flux, the relative role of convective area fraction and vertical velocity on mass flux, and the sensitivity of vertical velocity and mass flux profiles to changes in thermodynamics conditions. Efforts along these lines may act as a pure observational complement to help anchor other recent GCM convective parameterization environmental forcing and closure studies [e.g., *Suhas and Zhang*, 2015].

This study makes use of an extended convective data set collected within the Amazon basin during the Observations and Modeling of the Green Ocean Amazon (GoAmazon2014/5) Experiment [*Martin et al*., 2015, 2016]. The Amazon basin features prolific rain producing conditions under relatively "wet" (December to March) and "dry" (June through September) regimes, spanning a variety of cloud and precipitation types. The regimes and their transitions are related to the differences in the thermodynamic forcing for convection controlled by surface heat fluxes and large-scale moisture transport [e.g., *Li and Fu*, 2004; *Fu and Li*, 2004]. The breadth of cloud and precipitation frequency over the Amazon region, coupled with current GCM model inability to adequately represent convective cloud features over tropical areas, makes an extended Amazon deployment an important asset for understanding and improving GCM convective parameterization and associated feedbacks [e.g., *Williams et al*., 2002; *Richter and Xie*, 2008]. As part of GoAmazon2014/5, the Atmospheric Radiation Measurement (ARM) Mobile Facility (AMF) [*Miller et al*., 2016] collected a unique set of observations near Manacapuru, Brazil, a site known to experience both the pristine condition of its locale, as well as the effects of the Manaus, Brazil, mega city pollution plume. The AMF was equipped to capture a continuous record

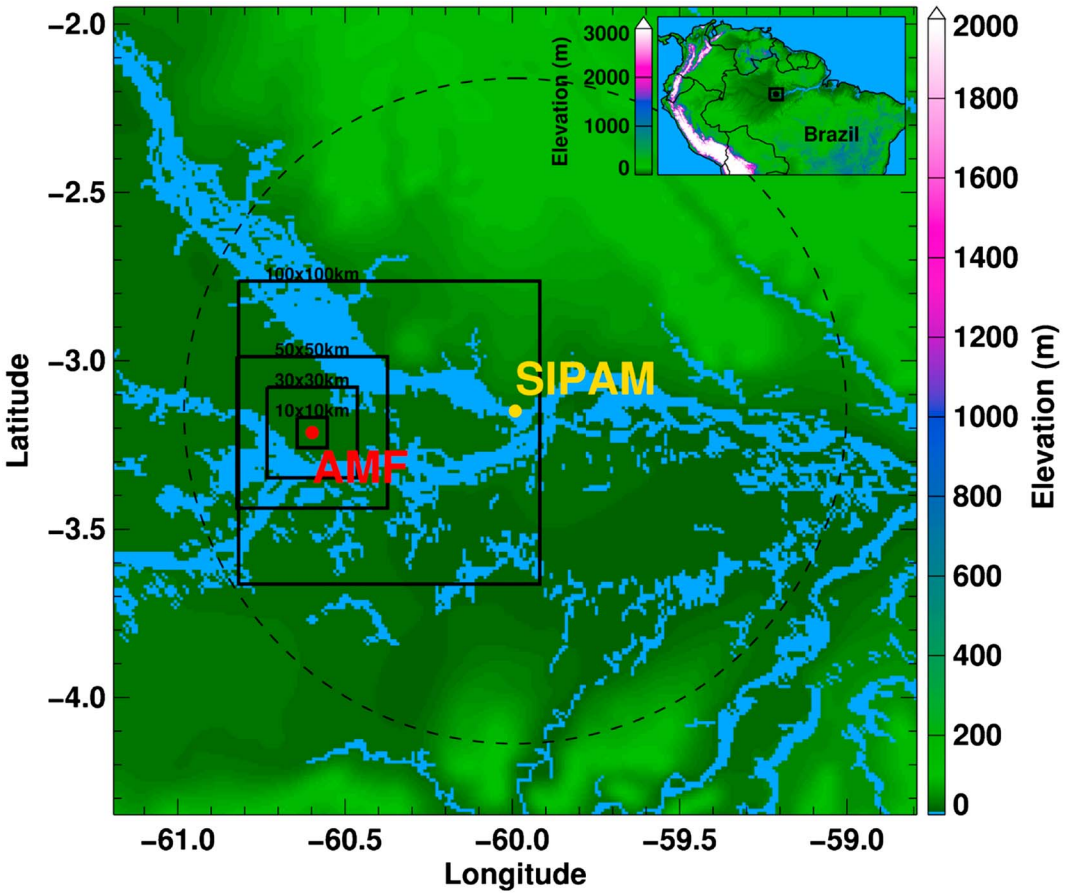

Figure 1. Map showing the location of the ARM AMF site near Manacapuru, Brazil, during GoAmazon2014/5. The AMF site is under the umbrella of the SIPAM conventional radar near Manaus, Brazil (dashed line 110 km radius range ring). Boxes represent the domains used in section 3.3 to test RWP sampling representativeness.

of column cloud properties from multiple radars, while frequent radiosonde launches help characterize convective forcing [e.g., *Xie et al*., 2015]. The AMF site is under the umbrella of the distributed System for the Protection of Amazonia (SIPAM) S band (3 GHz) conventional Doppler radar network that gives additional context for convective events summarized in this study [*Martin et al*., 2015].

The paper is outlined as follows. An overview of the GoAmazon2014/5 data set is presented in section 2. Methods to retrieve environmental parameters and GCM-scale vertical velocity, convective area fraction, and mass flux profiles are summarized in section 3. Results and breakdowns for this GoAmazon2014/5 data set, including activities to isolate the role of environmental forcing on these profiles, are presented in section 4. An extended discussion of the environmental breakdowns of convective core properties is found in section 5, and our key findings are summarized in section 6.

2. The GoAmazon2014/5 Data Set

As part of GoAmazon2014/5, the ARM AMF was positioned near Manacapuru, Brazil (Figure 1, herein T3 site). The data set includes near-continuous profiling observations over a period from March 2014 through December 2015. This study emphasizes cumulus congestus to deeper convective cloud properties observable by the RWP. These clouds typically have reflectivity factor Z values greater than 10 dBZ and are associated with much of the precipitation observed over the Amazon basin. We analyze convective properties from over 200 days of RWP observations that collected at least 5 min of measureable convective precipitation over T3. Convective precipitation is designated using a RWP-based echo classification approach described in section 2.1. These convective precipitation observations occur within the hours we define as "when convection is present" for the area fraction and mass flux calculations performed by this study.

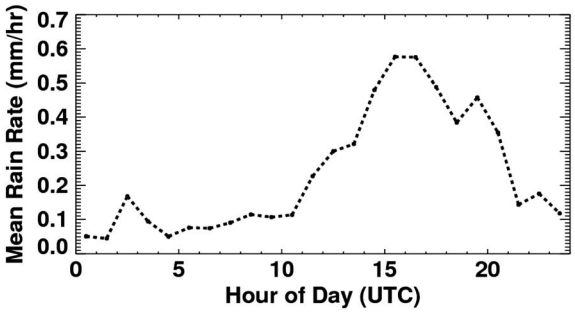

Figure 2. Diurnal cycle of precipitation over the T3 site as estimated by the collocated tipping bucket rain gauge.

Gauge-based rainfall accumulations coupled with the RWP during GoAmazon2014/5 indicate that convective cloud echoes occupy 35% of the available RWP observations (when any rain is measured) and contribute roughly 70% of the total rainfall accumulation (>3000 mm total data set precipitation). Wet and dry season precipitation at T3 adhered to established local diurnal cycle controls that are highlighted by the quasi-regular timing for early afternoon convection between 1500 and 1800 UTC (local noon—3 pm, Figure 2). Larger-scale thermodynamical shifts between the wet and dry seasons promote additional complexity, including initiation of propagating mesoscale convective systems that introduce overnight widespread stratiform rain contributions. However, most widespread precipitation contributions over T3 are limited, observed during transitional periods and sea breeze front intrusions into the basin [*Romatschke and Houze*, 2010; *Burleyson et al*., 2016].

2.1. The Radar Data Set

The ARM 1290 MHz UHF RWP is the primary instrument for retrievals. This RWP was reconfigured for precipitation modes similar to an S band radar profiler [e.g., *Atmospheric Radiation Measurement*, *ARM Climate Research Facility*, 2009; *Williams*, 2012; *Giangrande et al*., 2013; *Tridon et al*., 2013]. The beam width is large (6°, e.g., ~ 1 km at 10 km above ground level (agl)); however, vertical and temporal resolutions (200 m and 5 s, respectively) are reasonable for convective studies. RWP reflectivity factor measurements and vertical velocity retrieval examples for a 20 March 2014 event are shown in Figure 3. A collocated W band ARM Cloud Radar [e.g., *Atmospheric Radiation Measurement*, *ARM Climate Research Facility*, 2005; *Giangrande et al*., 2010, 2012] is consulted to help ensure we are mitigating clutter in RWP data sets associated with Bragg echoes.

The closest surveillance SIPAM radar was located 67.8 km northeast of T3. This radar provides grazing angle coverage useful to generate composite constant altitude low-level gridded reflectivity maps (e.g., constant altitude plan position indicators, CAPPIs) for convective area fraction estimates over domains comparable in size to a GCM gridbox. An overlapping SIPAM data set was available from March 2014 to May 2015, sufficient to establish the statistical representativeness of T3 column observations (section 3.3). The SIPAM radar data (1.8° beam width) were gridded to a Cartesian coordinate grid with horizontal and vertical resolution of 2 km and 0.5 km, respectively. A texture-based classification method [*Steiner et al*., 1995] was applied to the 2.5 km altitude reflectivity CAPPI, updated every 12 min, to designate convective echoes. The 1-hourly SIPAM convective area fractions for several representative GCM gridbox sizes were then estimated (domains as outlined on Figure 1). Finally, the use of SIPAM data was limited to a 110 km radius from the radar (dashed circle, Figure 1). Beyond this range, data collected during certain months were occasionally unreliable. Thus, the largest 100 km domain box was moved eastward by 25 km to accommodate this change.

2.2. Disdrometer Data Set

Five minute aggregate drop size distribution (DSD) measurements are obtained from a Parsivel unit using standard ARM drop censoring and processing techniques [e.g., *Atmospheric Radiation Measurement, ARM Climate Research Facility*, 2006; *Tokay et al*., 2013; *Giangrande et al*., 2014]. The disdrometer provided a routine calibration reference for the RWP Z estimates (to within 1–2 dB), as required for power law relationships used to estimate the hydrometeor fall speed contribution to the retrieved RWP vertical motion estimate (discussed in section 3). Rainfall speed power law relationships were also evaluated with Parsivel DSDs, using an assumption that the near-surface ambient vertical air motion is negligible. Those efforts follow a *Steiner* [1991] relationship form, $V_t = aZ^b$, where V_t is in (m s^{-1}), Z is in linear units (mm^6 m^{-3}), the "b" coefficient is fixed at 0.098, and the "a" coefficient is estimated as 2.65 m s^{-1} when using the convective rain DSDs collected during GoAmazon2014/5.

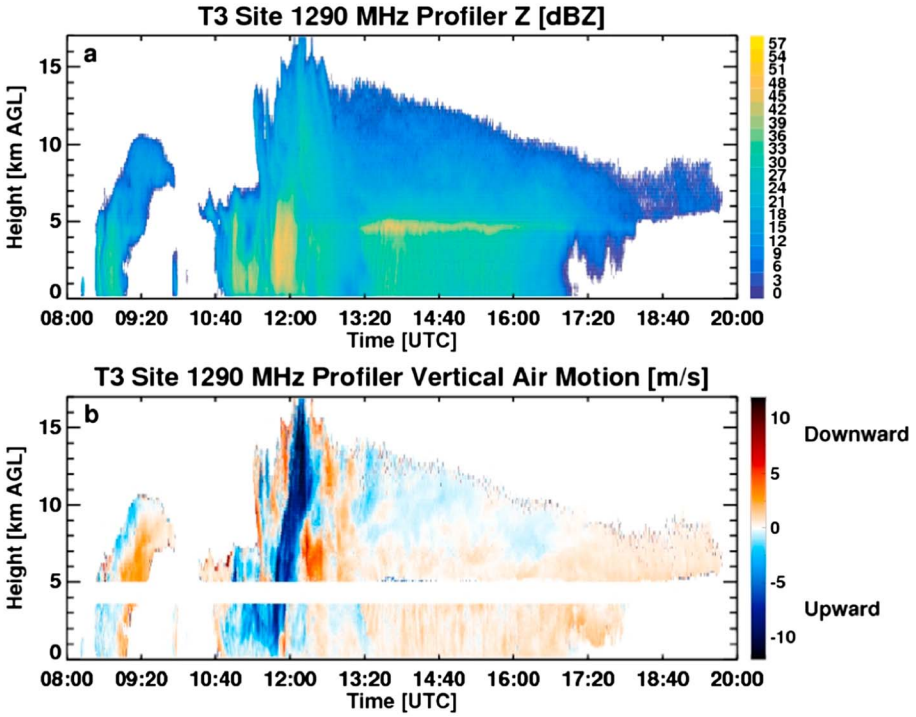

Figure 3. Example (a) reflectivity factor *Z* measurements and (b) vertical velocity retrievals from the 20 March 2014 event during GoAmazon2014/5.

2.3. Radiosondes

Radiosondes were launched over T3 at regular 6 h intervals. Basic thermodynamic processing was performed following *Jensen et al*. [2015] to estimate common thermodynamic/environment quantities of interest including convective available potential energy (CAPE) and convective inhibition (CIN). Based on the diurnal cycle of precipitation (Figure 2), the closest preconvective environment sounding was typically obtained from the launches between 1100 and 1200 UTC (approximately 8 A.M. LT) and used to estimate the environmental forcing controls. If unavailable, an earlier 0500–0600 UTC (approximately 2 A.M. LT) sounding was inserted. Figure 4 plots summary frequency histograms for the surface-based CAPE (mean ~ 1768 J kg^{-1} K^{-1}), CIN (mean ~ −60 J kg^{-1} K^{-1}), and low-level (0–5 km) mean relative humidity RH (mean ~ 76%) for our data set. Solid lines on Figure 4 indicate the median data set values, while dashed lines represent one standard deviation from the data set mean. The standard deviations for CAPE, CIN, and RH are found as 887 J kg^{-1} K^{-1}, 45 J kg^{-1} K^{-1}, and 9%, respectively. As the mean and median values are similar, mean values provide the primary reference point used to segregate favorable from unfavorable thermodynamical conditions in section 4. Distributions of the most unstable CAPE (mean ~ 1963 J kg^{-1} K^{-1}) and least stable CIN (mean ~ −36 J kg^{-1} K^{-1}) are also estimated but not emphasized in this study owing to similar relative distributions and standard deviations for data set breakdowns.

3. Methodology and Additional Considerations

Although scanning radar networks are suitable to identify convection over large domains, these networks typically do not prioritize placement and scanning useful to routinely retrieve vertical wind estimates. Meanwhile, profilers capture vertical velocity within an atmospheric column but must sample over long periods to yield useful convective information on updraft and downdraft distributions. One goal is to estimate convective vertical velocity and mass flux profiles that represent the composite of the vertical velocities inside all convective clouds within a representative GCM-scale grid. *Kumar et al*. [2015] argued that this could be accomplished using profilers by assuming that the ensemble averages performed on a long time series of profiler observations (e.g., many 3 h samples) should approximate the ensembles drawn from convective properties collected over large spatiotemporal domains (e.g., 60 × 60 km). By coupling a profiler site with a

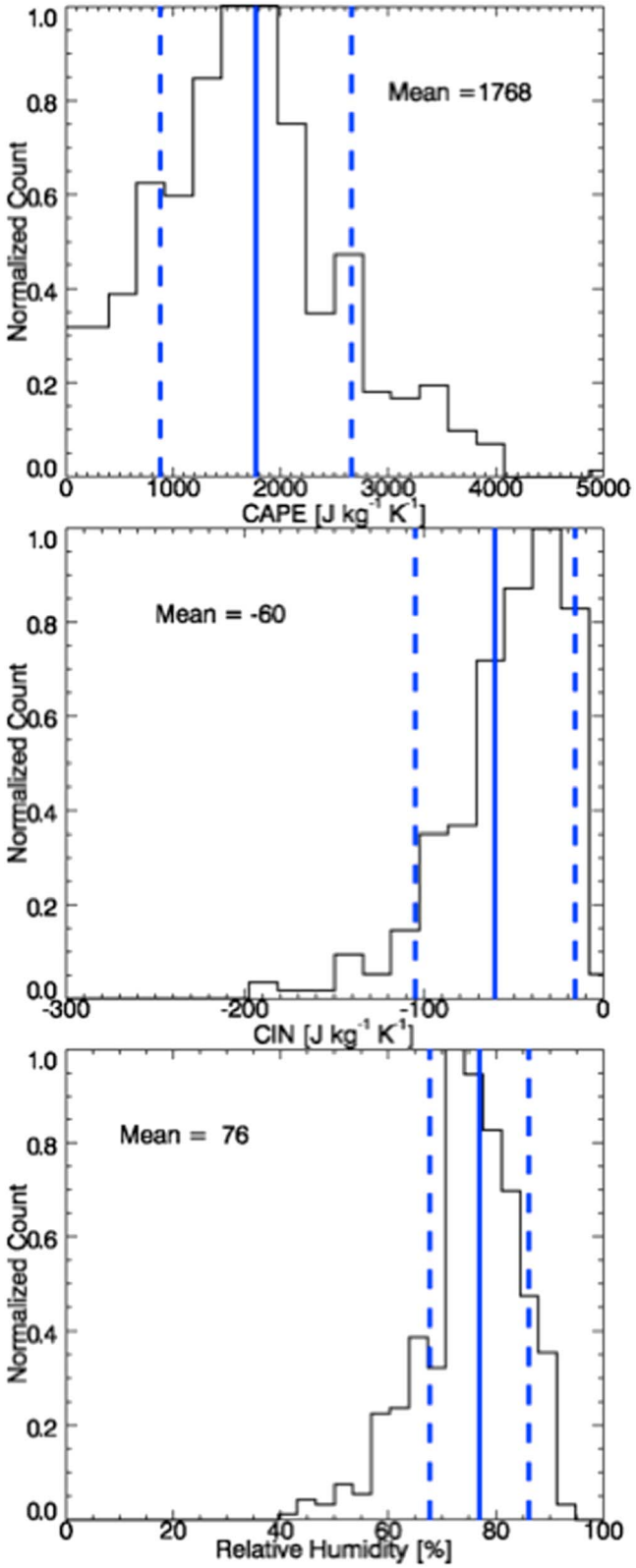

Figure 4. Frequency histograms for the surface-based CAPE, CIN, and low level (0–5 km) mean relative humidity RH (%) for event days in this study. Solid lines indicate the median values. Dashed lines indicate one standard deviation from the data set mean.

surveillance radar, *Kumar et al*. [2015] attempted to give confidence for this assumption by finding that the ensemble average point convective fractions over a Darwin profiler were similar to those from the larger scanning radar horizontal domain.

3.1. Profiler Estimates of Vertical Velocity in Convection

Air motions retrievals in precipitation are performed following *Giangrande et al*. [2013] using minor modifications for tropical Amazon thunderstorms (e.g., Figure 3). These retrievals follow two basic steps. First, echo classification is used to identify the RWP convective columns of interest. Since RWP mean Doppler velocity measurements reflect contributions from ambient air motions and particle fall speeds, the second step is to account for these hydrometeor fall speed contributions by using power law relations and freezing level height to estimate the vertical air motion at a given RWP range gate.

Our standard RWP preprocessing includes a fuzzy-logic echo classification following *Giangrande et al*. [2013], similar to methods previously described by *Geerts and Dawei* [2004] and *Lerach et al*. [2010]. Vertical columns are designated as "convection," including the extension into weaker echo regions aloft (where radar returns may drop below traditional radar-based convective echo thresholds). Columns with traditional radar bright band signatures [e.g., *Fabry and Zawadzki*, 1995] are excluded from classification as convection. However, additional checks are performed on the remaining columns to include any nonbright band column having a maximum $Z > 35$ dBZ and/or an absolute mean Doppler velocity value above the freezing level > 5 m s^{-1} as convection. Periphery anvil or adjacent cloud columns that do not exhibit coherent precipitation signatures to the surface are not included.

Below the freezing level, rainfall speed adjustments follow relations obtained from the local disdrometer

measurements (section 2.2). Unlike previous efforts [*Giangrande et al.*, 2013], hail contamination above or below the freezing level is not considered as a significant source of retrieval uncertainty during GoAmazon2014/5. Instead, most retrieval uncertainty (1–2 m s^{-1}) is attributed to the power law fall speed relations used to correct for graupel and/or mixed phase media in convective cores above the freezing level, and the conditions for which those relationships are applicable. From previous Oklahoma studies in *Giangrande et al.* [2013], a theoretical power law relationship was established using Oklahoma-matched model outputs (having variable graupel density) as $V_t = 2.2 + \sqrt{\left(10^{[(Z[\mathrm{dBZ}]-33)/10]}\right)}$, where V_t is in (m s^{-1}). However, sensitivity testing for this fall speed relation during the tropical Amazon deployment identified that a modification to $V_t = 2.3 + \sqrt{\left(10^{[(Z[\mathrm{dBZ}]-30)/10]}\right)}$ better aligned with a longer-term statistical profile expectation for decreasing downdraft frequency with altitude.

Physically, the adjustments to *Giangrande et al.* [2013] methods described above may be interpreted as follows: At very small radar reflectivity $Z < 25$ dBZ associated with smaller- and/or low-density particles, the change in predicted fall speed is negligible. As Z increases in elevated cores, this change (to within 1 m s^{-1}) would be consistent with Amazon storms indicative of a higher propensity of small, faster-falling mixed-phase particles ($25 < Z < 35$ dBZ). Since this retrieval method assumes mixed-phase media does not fall faster than liquid having the same Z, cores with $Z > 35$ dBZ at this crossover point revert to the rainfall speed behavior. For $Z > 35$ dBZ, the differences are also to within 1 m s^{-1}, the change favoring lower density, slower falling particles for continental Oklahoma cores having approximate $35 < Z < 45$ dBZ.

To help illustrate the appropriateness for statistical mixed-phase relationship changes due to natural variability in tropical regimes, one option is to compare these Amazon relationships against dual-frequency wind profiler retrievals performed from Darwin (50 MHz and 920 MHz, as in *Protat and Williams* [2011] and *Williams* [2012]). Unlike single-frequency RWP-based GoAmazon2014/5 retrievals, dual-frequency retrievals from Darwin directly measure the vertical air motion (using the 50 MHz profiler) and the mean Doppler velocity (using the 920 MHz profiler). While the strengths and weaknesses for single- versus dual-frequency methods are beyond the scope of this study, one strength of the dual-frequency approach is that statistical hydrometeor fall speed behaviors can be estimated as a residual. Figure 5 depicts one example for the dual-frequency retrieval approach applied to a tropical, weak convective Darwin monsoon event. The frequency scatterplot in Figure 5 highlights fall speed retrievals from 5.5 km to 7.5 km (adjusted to surface) against the associated bulk 920 MHz RWP Z estimate. The Amazon convective power law fall speed relationships for graupel (red line, $Z < 35$ dBZ) and rain (dashed line, $Z > 35$ dBZ) are overlaid. For this case (and many within the Darwin tropical monsoon), the Amazon curves we adopt are well matched to tropical Darwin convective core observations. For additional reference, a widespread stratiform dry aggregate snow matched subset $V_t = 0.37Z^{0.19}$ (blue line) is also observed and in line with nonspherical ice crystal expectations [e.g., *Hong*, 2007] yet distinct from convective core fall speed behaviors. Although supportive for these changes for tropical Amazon studies, these activities require future investigation. For instance, stronger updraft convective Darwin "break" monsoonal events do not exhibit similar agreement to larger values of $Z > 30$ dBZ and more closely follow continental Oklahoma relationships (e.g., presence of lower density ice particles).

3.2. GCM-Scale Mass Flux Ensemble Profile Estimation

Following *Kumar et al.* [2015], convective area fraction and vertical velocity profiles from a single column can be combined to calculate a mass flux M_c (kg s^{-1} m^{-2}). The mass flux M_c follows a traditional GCM-type definition that aggregates all convective clouds within a particular-sized domain:

$$M_c = \rho\sigma_u v_u + \rho\sigma_d v_d, \tag{1}$$

where ρ is the air density (kg m^{-3}) and σ_u is the horizontal area fraction covered by updraft cores in the grid-box (dimensionless, ratio of the "updraft" area to the total domain area), v_u is the mean updraft velocity (m s^{-1}), and σ_d and v_d are similar quantities for the area fraction and mean velocity of the downdraft cores, respectively. In equation (1), mean profiles may be computed from the RWP over temporal aggregation intervals deemed appropriate for GCM-type comparisons (section 3.3). All convective regions designated by the RWP (i.e., $|v| \geq 0$ m s^{-1}, no thresholds) are classified as an updraft or downdraft. By avoiding the use of core length or significance thresholds, *Kumar et al.* [2015] argued these composite profile retrievals to be in better alignment with GCM outputs.

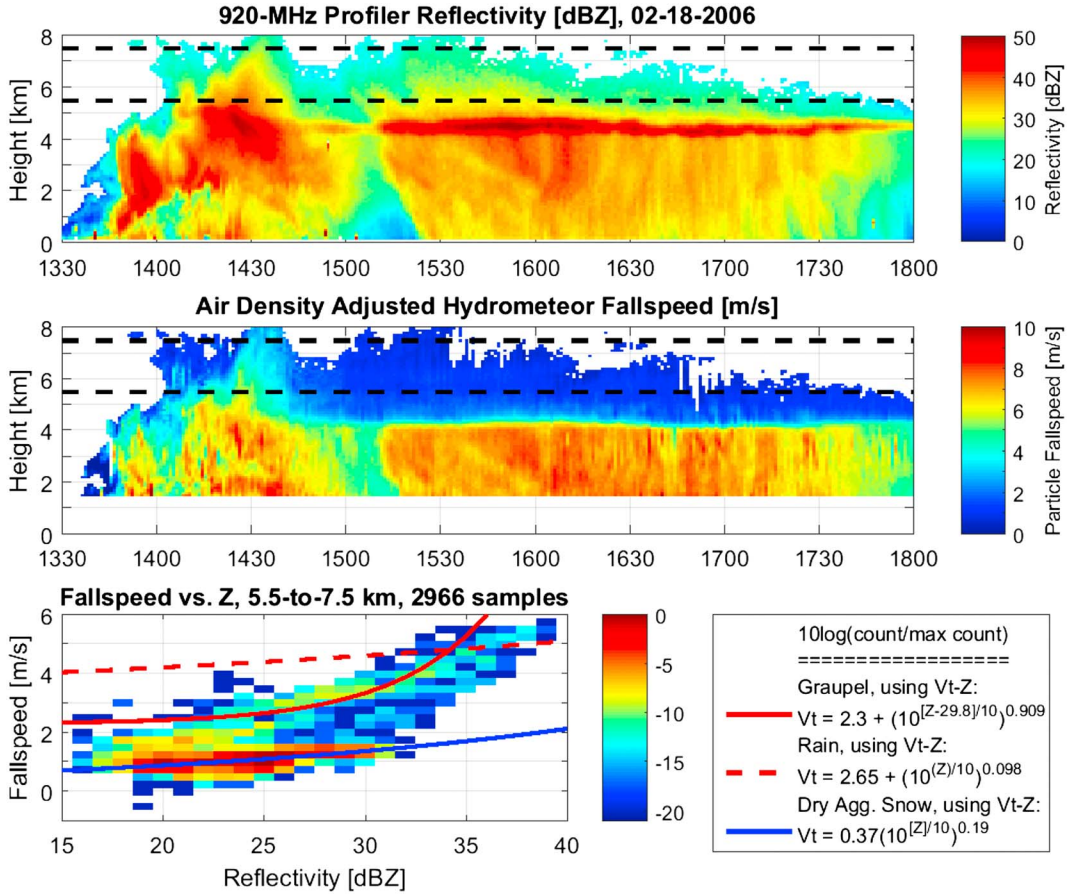

Figure 5. Results from the 18 February 2006 event as viewed by the Darwin, Australia, dual-frequency profiler. (top) 920 MHz Reflectivity, (middle) surface-adjusted hydrometeor fall speed retrievals, and the (bottom) coupled cumulative frequency scatterplots for *Z* and fall speed drawn from the observations between 5.5 km to 7.5 km. Solid red line in Figure 5 (bottom) is the graupel/mixed-phase power law relationship applied for the Amazon in this study. Dashed red line is the rain power law relation as matched using the Amazon Parsivel data set for convective cells. Blue line represents a matched "aggregate snow" relation as observed in regions outside convective cores.

As reported by *Kumar et al.* [2015], initial sensitivity testing revealed that mean mass flux profiles calculated using equation (1) were relatively robust to minor modifications in convective echo classification and/or core significance thresholds. As an example, if a more stringent convective echo classification were implemented, this would lead to a decrease in the fractional convective area. We also find that this decrease was roughly compensated in mean mass flux profile behaviors (section 4) by an increase in the mean velocity over the remaining regions. One basic interpretation for this may be tied to velocities in convective core regions. This behavior fits with core velocities that vary smoothly from peak "core" intensity out to the peripheries (e.g., triangular updraft plume assumptions).

3.3. Representativeness of RWP Sampling to GCM Gridbox Sizes

As with *Kumar et al.* [2015], this study must determine whether the time mean RWP properties and ensemble averages are approximately representative of area mean quantities for GoAmazon2014/5. One basic approach that follows the *Kumar et al.* [2015] study is to compare average ensemble convective cloud properties as sampled by the SIPAM radar, capable of capturing point-to-larger-scale convective area coverage. Testing is performed over the T3 RWP site that is isolated and removed from several lower level contaminants (e.g., ground clutter and blockages). Figure 6 plots a summary SIPAM convective occurrence as derived from 2.5 km agl CAPPI measurements. This plot summarizes the wet season months (December to March) at the most active 3 h interval (15–18 UTC). The example highlights that convection is often most frequent over land surfaces (removed from underlying river influences, consistent with *Burleyson et al.* [2016]) and that it occurs at a frequency between 2% and 7% during the 3 h interval most favorable to convective development.

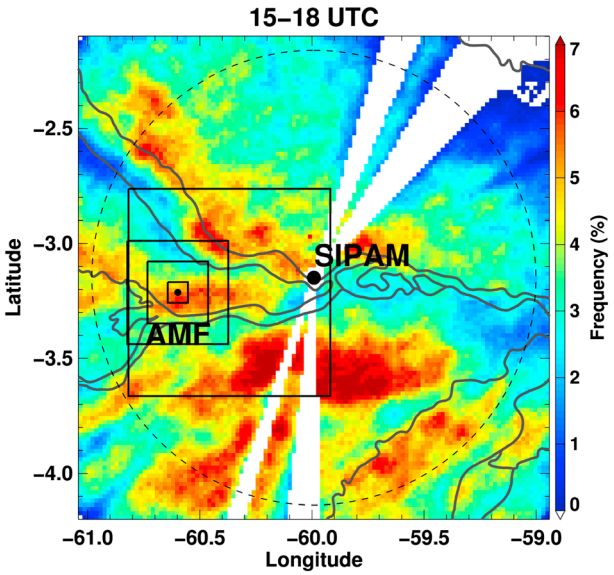

Figure 6. Mean convective area frequency of occurrence as designated by SIPAM radar during GoAmazon2014/5 wet season events (December to March) for the 3 h window between 15 and 18 UTC. Blocked radials are masked and not included in fractional area calculations.

Deriving GCM grid-scale properties from vertical profiles is a challenging task [e.g., *Illingworth et al.*, 2007]. One proxy is to reconstruct a 2-D vertical cross section using the RWP by including all profiles sampled over a time interval that corresponds to the GCM grid length. In order to do so, the propagation speed of the convective cells is used to "convert" this grid length to a time span. The main assumption is then that the obtained set of profiles is statistically representative of the whole volume of the GCM grid scale. An average propagation speed of $5\,m\,s^{-1}$ is assumed for Amazon convective cells, as estimated using SIPAM cell tracking algorithms such as those presented in *Vila et al.* [2008]. Based on this average propagation speed, a 1 h time-height RWP column behavior (e.g., the mean convective area fraction profile) maps to a spatial grid domain of approximately 20 km. In a similar fashion, a 3 h (6 h) column-time interval would roughly translate to a spatial grid domain of 60 km (120). Since 20 km to 100 km grids reflect conventional to next-generation GCM grid resolution, initial focus is on the representativeness of 1 h, 3 h, and 6 h RWP column behaviors and the compositing therein. These tests cover a wide range of possible options when approximating the spatiotemporal averages collected from larger horizontal domains.

Average convective area fractions for five different SIPAM spatiotemporal scales are tested over the gridboxes depicted on Figure 6. The horizontal scales we compare include point (native 2 km grid), 10 km, 30 km, 50 km, and 100 km. We include only the 1 h, 3 h, and 6 h intervals that have at least 60% of the available SIPAM volume scans (approximately 6000 one hour intervals from SIPAM) to ensure fidelity for spatiotemporal behaviors from point-to-spatial scales. When ensemble averaging over the entire SIPAM record across these five domain options and according to each time interval (1 h, 3 h, and 6 h), the mean SIPAM convective area fractions converge at approximately 2% (not shown). The result should not be surprising, since the basic interpretation is that the campaign experiences a convective rainfall event every few days, with the typical convective event lasting a few hours. Since most hours in the data set do not experience convective precipitation, the sequential ensemble averaging encourages all options to converge at a very small convective fraction (e.g., averaging a large number of zero values/zero padding). *Kumar et al.* [2015] drew from this logic to infer that ensemble convective profiles drawn from a lengthy set of 3-hourly profile averaging samples would be a good approximation for the average convective profile behavior observed to within a GCM-size gridbox.

However, the situations important to GCM model evaluation are often those drawn from specific intervals wherein convection initiates and is present over a GCM-like domain. To better inform on the representativeness of ensemble profiles, we can isolate the properties from 1 h and longer intervals according to the instances that a large GCM-like scale domain (~100 km) observes convection (independent of a RWP-point location "hit"). For this test, we consider only 1 h and longer intervals that featured a minimum 1% convective area fraction over the 100 km spatial domain scale (e.g., Table 1). Since convection is uncommon, this removes 70% of the previous data set. Retaining only the independent samples with convection in the vicinity of the T3 site results is an increase in the ensemble average convective area fraction, to approximately 6%. Area fraction is typically higher over the smaller, RWP-like domains. From Table 1, a modest (~1–2%) agreement persists when performing these SIPAM tests up to convective area fractions over 5–10% of the equivalent 100 km domain. Average convective area fractions deviate by more than 3–5% above those levels,

Table 1. Average SIPAM Data Set Convective Area Fractional Coverage for 1 h to 6 h Spatiotemporal Intervals Contingent on Coverage Thresholds for When Convection Is Present Over the Larger 100 km Domain

1% Area Coverage (100 km Domain)	Point/2 km Area Coverage (%)	10 km	30 km	50 km	100 km
1 h	6.6	6.6	5.95	5.7	5.9
3 h	5.9	5.9	5.3	5.0	5.2
6 h	4.9	4.9	4.4	4.2	4.4
5% Area Coverage (100 km Domain)	Point/2 km Area Coverage %	10 km	30 km	50 km	100 km
1 h	12.4	12.4	11.3	10.7	10.6
3 h	11.6	11.5	10.3	9.8	9.6
6 h	9.6	9.8	8.8	8.4	8.1
10% Area Coverage (100 km Domain)	Point/2 kmArea Coverage %	10 km	30 km	50 km	100 km
1 h	20.3	20.2	18.6	17.3	16.0
3 h	19.0	18.9	17.4	16.5	15.0
6 h	15.5	14.9	13.5	13.5	13.0

as also constrained by the limited number of events having convective area fractions exceeding 10% over the 100 km domain.

Many differences reported in Table 1 are allowable, since shorter temporal column behaviors including point-column 1 h average ensembles are only anticipated to be relevant to inform at approximate 20–30 km horizontal domain scales (or 3 h averages to 50–60 km scales, etc.). One may consider reversing the tests that were performed to confirm whether substantial precipitation over T3 would be consistent with substantial precipitation over the larger spatiotemporal domains; for example, we checked the consistency between the domains for events where the convective area fraction over the T3 (point) exceeded 10%. Once again, SIPAM ensemble averages were roughly aligned at appropriate scales.

Kumar et al. [2015] support the ensemble averaging of large populations of individual 3 h profiler samples to generate representative GCM-scale profiles. Therefore, it is instructive to consider the quality and natural variability found in that baseline (instantaneous) point-column sampling as compared to larger field-of-view (FOV) SIPAM samples. Similar to radar-based column cloud fraction studies [e.g., *Berg and Stull*, 2002], hourly convective area fraction averages obtained from the single-point (2 km) or limited area (10 km) SIPAM records are highly correlated (Pearson correlation coefficient $r \sim 0.9$) to the comparable hourly samples obtained over the largest matched (e.g., 30 km) SIPAM spatiotemporal domains. Comparisons of the instantaneous samples suggest low Bias (to within 1%) and a root-mean-square error RMSE (approximately 7%) associated with sampling (noise) and physical process limitations. When we consider lengthier 3 h and 6 h point-column comparisons against associated lengthier spatiotemporal FOVs (e.g., 50 km and 100 km), the correlations are lower ($r \sim 0.75$ and $r \sim 0.65$ for 3 h and 6 h, respectively), while the RMSE also decreases (6.1% and 4.5%, respectively). Since many Amazon convective events do not persist for longer than a few hours, the improvement in RMSE at the lengthier scales is attributed to some zero padding. Overall, these RMSE behaviors for convective area fraction imply that a relatively large number of samples would need to be averaged to ensure a low composite RMSE behavior (e.g., to within 1–2% convective area fraction). Random sampling from this data set (to avoid seasonal, sequential similarities) conservatively places this number of hourly samples on the order of 100. The number of required samples is reduced for longer sample windows, e.g., aided by zero padding.

At a glance, the testing follows previous examples by *Kumar et al*. [2015] and motivates that the T3 RWP location may be possibly representative when considering ensemble statistical behaviors. Although we initially considered from 1 h, 20 km × 20 km scales up to 6 h, 120 km × 120 km ensemble averages, there are concerns for using lengthier RWP samples as representative of larger domains. This is shown in the reduction of the sample correlations as discussed above and may include additional diurnal factors. Therefore, this study emphasizes 1 h and 3 h properties that are found to be in modest alignment and similar to the previous Darwin study. As in Figure 1, the T3 site is located at the confluence of the Amazon and Rio Negro Rivers, a region of strong underlying moisture [e.g., *Romatschke and Houze*, 2010]. Testing indicated bias favoring higher convective area fractions over the smaller, more local T3 domains. This may highlight an additional concern that the T3 location is a relative focal point for enhanced convection (coverage). The result aligns well with satellite-based deep convective cloud occurrence maps as in *Burleyson et al*. [2016]. Therefore, mass

Table 2. The 2 Year GoAmazon2014/5 Data Set Frequency of Convective Occurrence for 3 h Average Properties, Separated According To Environmental and Regime Conditions

Condition	# of 3 h Samples	Subset < Mean > Values
CAPE > 1770 J kg^{-1} K^{-1}	217	2450 J kg^{-1} K^{-1}
CAPE < 1770 J kg^{-1} K^{-1}	197	1075 J kg^{-1} K^{-1}
CIN > −60 J kg^{-1} K^{-1}	245	−30 J kg^{-1} K^{-1}
CIN < −60 J kg^{-1} K^{-1}	169	−104 J kg^{-1} K^{-1}
RH [0–5 km] > 77%	237	84%
RH [0–5 km] < 77%	177	69%
Dry season, Jun–Sept	103	CAPE: 1900 J kg^{-1} K^{-1} CIN: −74 J kg^{-1} K^{-1} RH: 70%
Wet season, Dec–Mar	154	CAPE: 1500 J kg^{-1} K^{-1} CIN: −58 J kg^{-1} K^{-1} RH: 79%
Total, 3 h events	414	CAPE: 1768 J kg^{-1} K^{-1} CIN: −60 J kg^{-1} K^{-1} RH: 76%

flux profiles as estimated by this study may also be enhanced as compared to the expectations over the larger Amazon basin.

4. Observational Breakdowns From the GoAmazon2014/5 Campaign

Ensemble mean convective profile behaviors and environmental separations are estimated from the RWP data set of 200 convective event days. The data set includes approximately 532 single hours (1 h) and 414 3-hourly periods (3 h) matching the when convection is present 5 min rainfall criteria. Overall, the Amazon events include an approximate 30% contribution from possible congestus clouds, defined as RWP convective columns having an echo top height (ETH) < 8 km [e.g., *Jensen and Del Genio*, 2006]. For the relative environmental forcing breakdowns in subsequent sections, only the results obtained from the 3 h, 60 km ensemble mean profiles are shown. This choice is made for simplicity, since the results at the 1 h scale are qualitatively similar and scale with area fraction. Data sets associated with these relative 3 h breakdowns are described in Table 2. The 3 h scale is also the closest matched to the previous *Kumar et al*. [2015] study for comparison purposes with Darwin observations.

4.1. Summary Amazon Convective Vertical Velocity, Area Fraction, and Mass Flux Profiles

Figure 7 plots data set summary 1 h and 3 h mean vertical profiles that translate to GCM scales of approximately 20 km and 60 km when assuming a 5 m s^{-1} cell propagation. Vertical velocity profiles in these plots represent a weighted-average behavior consistent with previous vertical velocity observational studies. Since any 1 h or 3 h window is not guaranteed to observe both updrafts and downdrafts, these profiles are weighted by the total number of velocity observations in the data set at a given altitude, not an ensemble average that considers each 1 h or 3 h sample equally important. Thus, there should be no significant difference between the profiles calculated at different scales. Qualitatively, vertical velocity profiles and maximum velocity properties in Figure 7 (top row) are similar to those found in previous studies [e.g., *May and Rajopadhyaya*, 1999; *Giangrande et al*., 2013]. Vertical velocity profiles for updrafts (red lines, positive) and downdrafts (blue lines, negative) increase with height, with peak magnitudes above 10 km. Observed maximum velocity values did not exceed 20 m s^{-1}. The overall convective profiles (black lines) are skewed toward updrafts at higher altitudes. Mean velocity magnitudes are lower than many previous studies [e.g., *LeMone and Zipser*, 1980; *Anderson et al*., 2005], but this is expected since those efforts draw profile properties only from cores meeting stringent significance thresholds.

For an aggregated vertical velocity depiction that better displays the spread of observed instantaneous velocities, a normalized cumulative velocity frequency with altitude display (CFAD) [e.g., *Yuter and Houze*, 1995] is plotted for the RWP data set (Figure 8a). Overlaid on this plot are the median (solid), 90th (dashed) and 95th (plus symbol) percentile velocity value profiles for the updrafts (positive) and downdrafts (negative). An advantage with CFAD depictions is that these normalized frequency observations are model scale independent. Again, we observe CFADs favoring more frequent and intense updrafts over downdrafts to higher

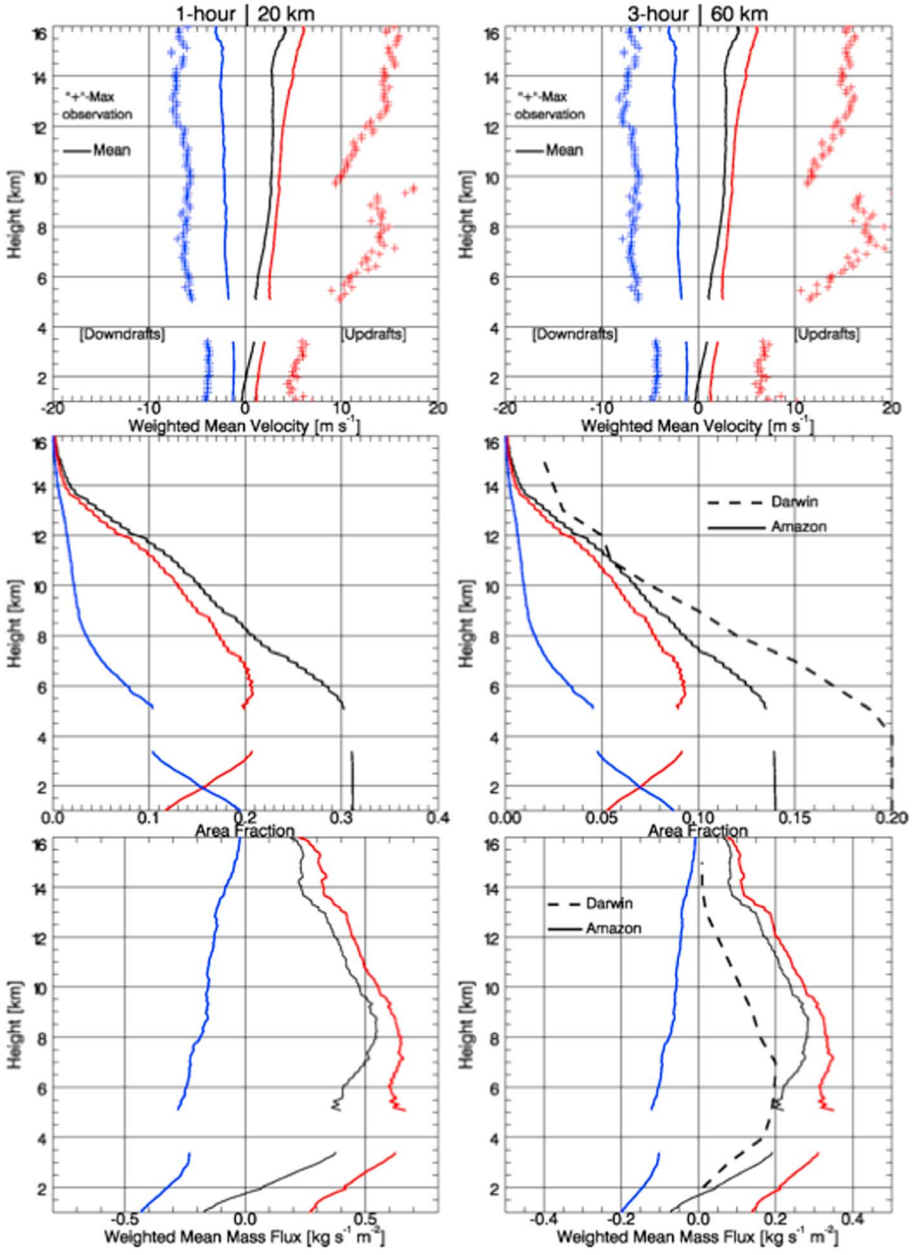

Figure 7. The (left column) 1 h and (right column) 3 h (top row) vertical velocity, (middle row) convective area fraction, and (bottom row) mass flux profiles for the GoAmazon2014/5 data set. Black lines represent ensemble mean properties, while red lines represent updraft properties and blue lines represent downdraft properties. Maximum velocities given by plus symbols. Dashed lines on the 3 h ensembles reflect the ensemble mean Darwin behaviors from *Kumar et al.* [2015].

altitudes. However, Figure 8 also highlights one motivation for improving longer-term velocity observational records. Longer data sets allow further control over these depictions for factors such as similar ETH conditions (as in Figure 8b, e.g., average ETH $>$ 12 km). From Figures 8a and 8b, we observe that the median vertical velocity profile is similar in magnitude and shape between the larger sampling and deeper clouds, as important for conventional mass flux estimates. However, increases in the 95th percentile magnitudes and other distribution changes at the higher altitudes within the deeper clouds may be of increasing interest to future GCM convective parameterization alternatives.

Figure 7 (middle row) plots the ensemble mean convective area fraction. The area fractions for the Amazon storms indicates a downward tendency from 30% average convective area coverage for the 1 h intervals

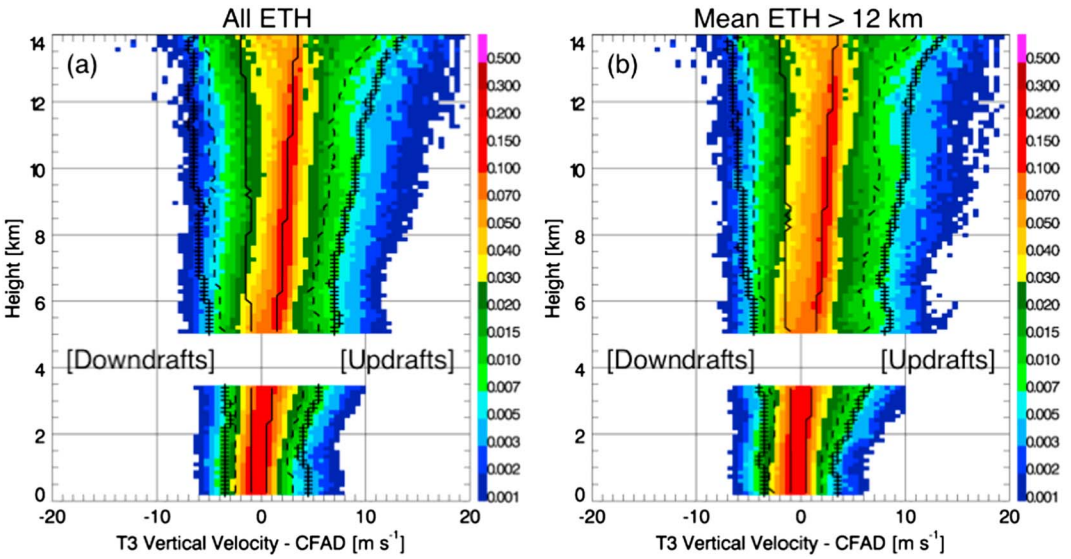

Figure 8. Normalized cumulative frequency histograms (CFADs) of vertical velocity for the GoAmazon2014/5 data set. Solid, dashed, and plus lines represent median, 90th and 95th percentile values. (a) Plot containing all convective vertical velocity instances. (b) Plot containing only those sample windows having mean echo top heights greater than 12 km.

when convection is present to approximately 14% coverage over the 3 h interval averages when convection is present. The profile shapes are qualitatively similar for updraft, downdraft, and total behaviors. Updraft area and updraft occurrence peak at the midlevels, whereas maximum downdraft area and maximum occurrence is at the lower altitudes. Updrafts occupy more area observed at all heights $>$ 2 km. Total convective area fraction (updrafts and downdrafts) decreases with increasing altitude owing to less frequent observations for the deeper cumulus clouds. One practical consideration (if comparing ensemble profiles to model ensemble behaviors) is that our definitions for including an RWP event in the ensemble averaging are important to the minimum convective area fraction we resolve. As before, this approach includes all event windows having 5 min of convective echoes to ensure we sample convection. For the 1 h scales, this implies an 8% minimum fractional area coverage. However, the criterion translates to a lower minimum ($<$3%) coverage requirement if aligning with ensemble model outputs at 3 h, 60 km scales.

Following equation (1), ensemble mean mass flux profiles are shown in Figure 7 (bottom row). The Amazon ensemble mass flux profiles increase from cloud base to a peak value near 8 km. The mean profiles are dominated by updrafts, with the exception at the lowest levels. For the 1 h domain-scale properties in Figure 7 (bottom row, left), ensemble mass flux profiles report similar profile shapes, but magnitudes that are approximately doubled those from the 3 h scale in Figure 7 (bottom row, right). Note that these properties scale with the differences in convective area fraction as observed in Figure 7 (middle row) that are also approximately doubled.

For reference to previous studies, the 3 h column in Figure 7 overlays mean profiles from the comparable 3 h observations over Darwin (adapted with permission from *Kumar et al*. [2015]). Note that since the Amazon vertical velocity profiles roughly overlap with those calculated for Darwin profiles in *Kumar et al*. [2015] having similar extended data set weighted mean averaging, these Darwin behaviors are not plotted in the top panel. Amazon and Darwin however indicate qualitatively similar convective area fraction profile shapes, with the ensemble Amazon convective area fractions observed to be lower until the upper levels. The ensemble mean mass flux profiles for Darwin are also overlaid, with the Amazon profiles reporting stronger mean mass flux to higher altitudes and profiles that peak at a higher relative altitude. This result implies stronger vertical velocities for Amazon storms, which may seem inconsistent with the limited contrasts we find between Darwin and Amazon weighted mean velocity profiles. Recall that those similarities may not be representative (unknown breakdown of events in the Darwin sampling), while contrasts may be difficult to observe when comparing only mean or median velocity profiles dominated by weaker velocities (as in Figure 8). Similarly, mass flux profiles give equal weight to each 3 h sample and are not dominated by samples that carry additional RWP observations.

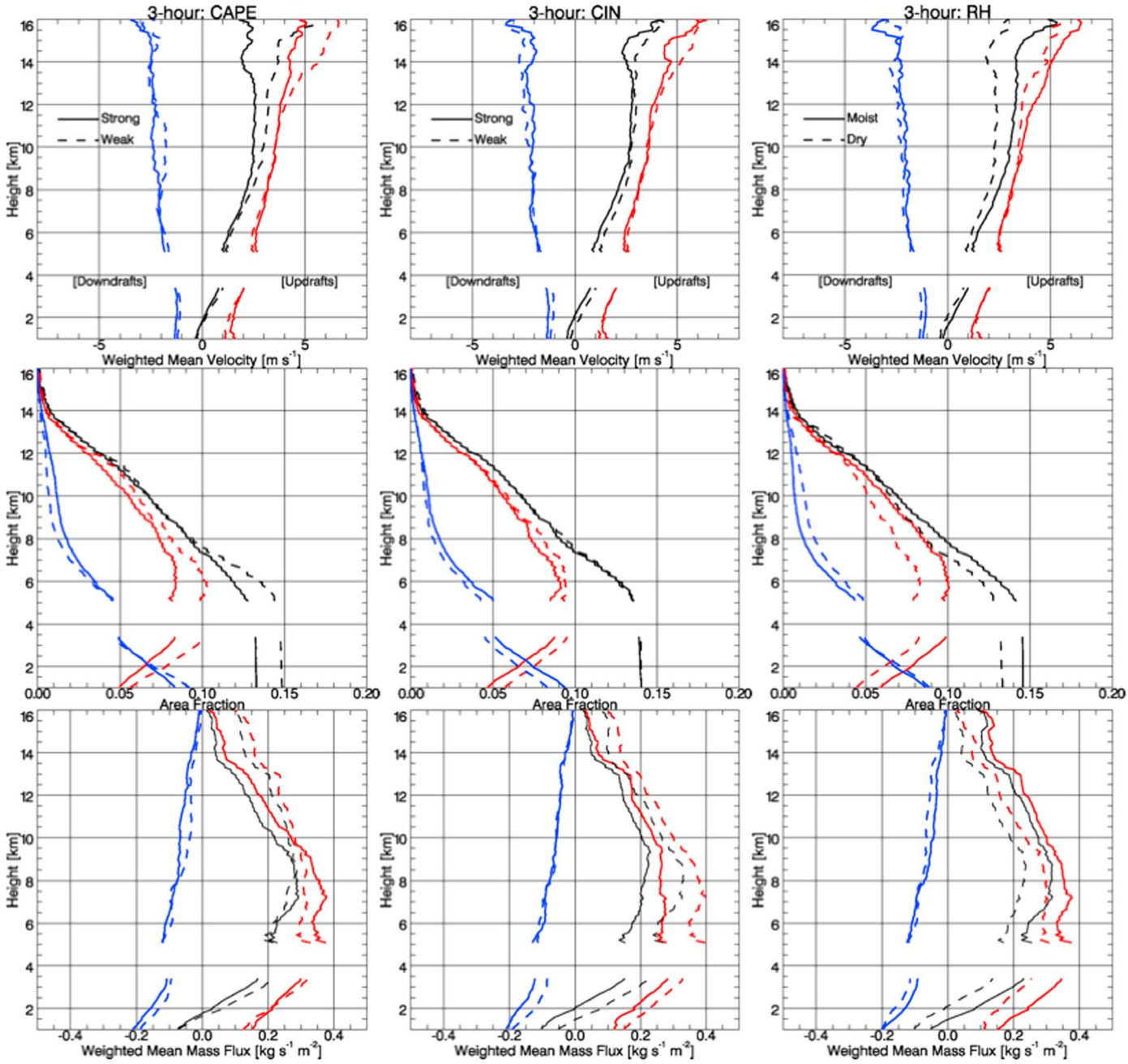

Figure 9. As in Figure 7 but for 3-hourly properties segregated according to the mean data set (left column) CAPE (1768 J kg^{-1} K^{-1}), (middle column) CIN (−60 J kg^{-1} K^{-1}), and (right column) low-level RH (76%) values. Stronger/moist conditions are represented by solid lines; weaker/drier conditions are represented by dashed lines.

4.2. Relative Mass Flux Profile Breakdowns According To Environmental Forcing

4.2.1. Role of CAPE on Mass Flux Ensemble Mean Profiles

Figure 9 (left column) displays ensemble mean profile breakdowns contingent on stronger (solid lines) and weaker (dashed lines) CAPE conditions (Table 2). These conditions are separated by the mean data set CAPE value when convection is present ~ 1768 J kg^{-1} K^{-1} (e.g., Figure 4a). Our use of "strong/weak" terminology for CAPE values is a relative, as all CAPE values for this data set are associated with convection. The average CAPE for the samples collected above the data set mean value was 2450 J kg^{-1} K^{-1}, while this value was 1075 J kg^{-1} K^{-1} for the samples below the data set mean CAPE. The updraft mass flux profiles (Figure 9, bottom row left) deviate at midlevel altitudes, with the net updraft mass flux profile similar or slightly

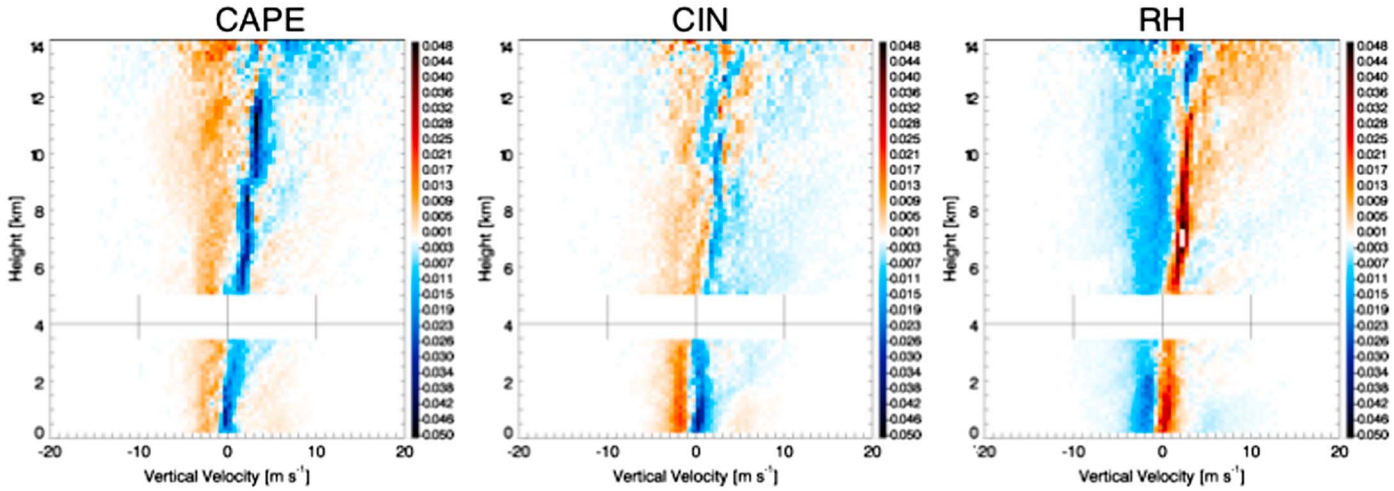

Figure 10. CFAD difference plots, for behaviors segregated according to CAPE, CIN, and low-level RH conditions, as based on data set mean values (as also in Figure 9). Red colors and/or positive values indicate that stronger/moister conditions are more frequently observed; blue colors and/or negative values indicate that weaker/drier conditions are more frequent.

enhanced under the stronger CAPE conditions to most levels below 10 km. Profile behavior reverses above 10 km for this data set, showing stronger upward vertical motions and mass flux for the weaker CAPE conditions.

To better interpret mass flux profiles and help constrain convective configurations that potentially attempt to match these behaviors, it is important to consult relative area fraction and vertical velocity breakdowns. First, total convective area fractions are lower (~13%) under higher CAPE conditions to all levels. This is mostly attributed to changes in updraft area, not downdraft areas, since the downdraft area is similar or slightly elevated under stronger CAPE conditions. We note that downdraft frequency is in reference to convective downdrafts only, and our definitions ignore widespread downward mass flux associated with stratiform regions. Since mass flux is the product of area fraction and velocity, this indicates that the associated similar or stronger mean updraft mass flux profiles observed to 10 km under heightened CAPE conditions are likely achieved by stronger updrafts (fewer, but stronger). Thus, stronger vertical motions observed to 10 km would be anticipated, although this is not immediately apparent from our use of weighted mean updraft profiles in Figure 9. Above 10 km, we observe stronger weighted mean updraft velocity profiles for relatively weaker CAPE conditions. This interpretation is straightforward, since stronger updraft velocities drive higher mass flux profile estimates (for similar convective area fraction). As following convective area fraction profiles, convective observations (predominantly updrafts) peak around 6 km and decrease rapidly above 10 km. Thus, additional uncertainty in profile observations to higher altitudes may be expected based on the limited number of samples (e.g., less than 30% of the observations are available above 12 km as compared with 6 km).

Since weighted mean vertical velocity profiles are dominated by the large number of small velocity values sampled by the RWP to lower altitudes, and possible sampling from a limited number of stronger events to higher altitudes, it is informative to consult the changes in CFAD behaviors. The difference according to stronger and weaker CAPE conditions is plotted along Figure 10 (left). From this difference plot, it is better shown that stronger CAPE regimes favor more diverse and stronger velocity distributions to higher altitudes below 10 km. Moreover, weaker CAPE conditions (blue) have the more pronounced distribution peaks confined to a narrower, slightly upward skewed vertical velocity distribution. Above 10 km, the narrow peak remains, and we observe evidence for a transition to stronger updrafts under relatively weaker CAPE conditions. Above 12 km, updrafts are favored under weaker CAPE conditions; however, the spread in CFAD velocity signatures may support our suggestion that data set sampling above 12 km is limited.

4.2.2. Role of CIN on Mass Flux Ensemble Mean Profiles

Profile behaviors are also segregated according to stronger (solid lines) and weaker (dashed lines) CIN conditions based on the mean data set value ~ $-60\,J\,kg^{-1}\,K^{-1}$ (Figure 9, middle column). The average CIN for the samples collected above the data set mean value was $-103\,J\,kg^{-1}\,K^{-1}$, while this value was

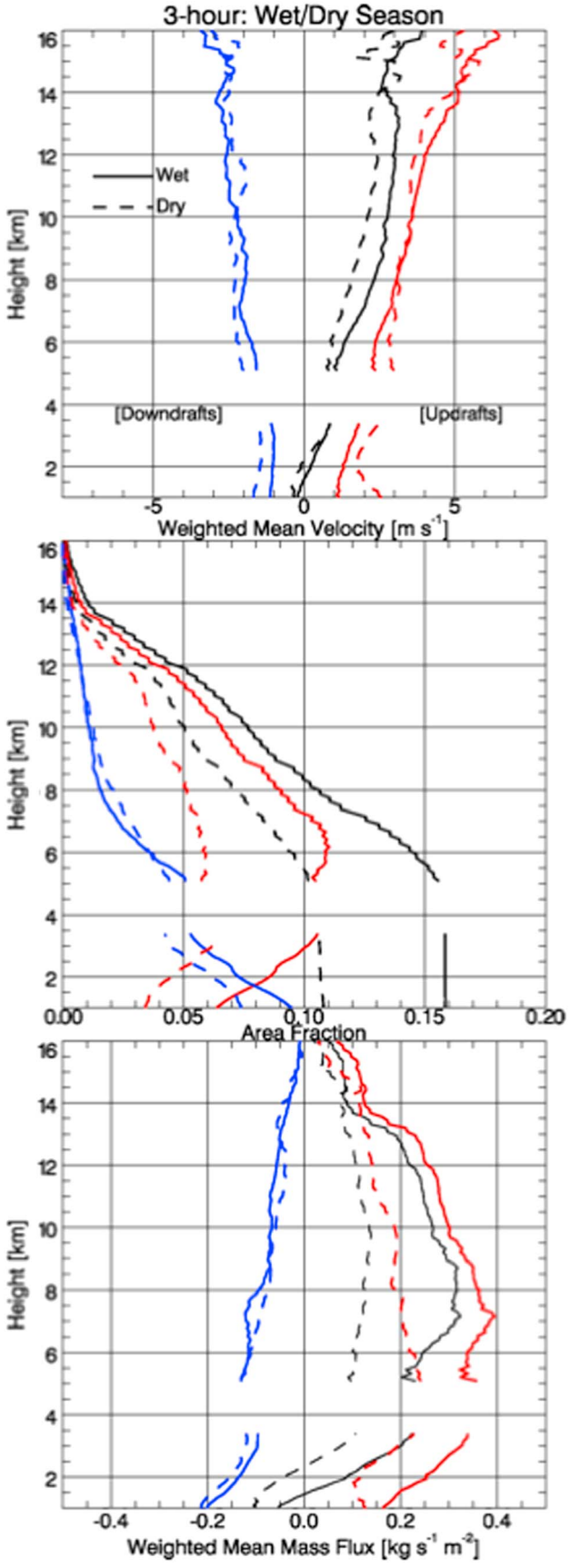

$-30\,J\,kg^{-1}\,K^{-1}$ for the samples collected below our data set mean CIN. Weaker, or smaller negative CIN conditions, exhibit higher total and updraft area fractions and possibly encourage stronger mean updraft vertical velocities. Those factors support the observed increases in convective mass flux profiles under weaker CIN conditions. Mass flux profiles also possibly suggest the favorable role for deeper storms under weaker CIN conditions, as based on the more pronounced peak location in mass flux profiles. As following the previous CAPE breakdowns, Figure 10 (middle) plots a CFAD difference plot corresponding to these CIN regimes (similar scales). Unlike the previous CAPE comparisons, contrasts in velocity and area fraction profiles under different CIN conditions are less conclusive; stronger CIN is apparently linked with more diverse convective downdrafts (although mean convective downdraft area fraction and mass flux are nominally similar), whereas weaker CIN is also linked with stronger and more diverse updrafts with mass flux peaked to higher altitudes.

4.2.3. Role of Low-Level (0 km–5 km) Relative Humidity on Mass Flux Ensemble Mean Profiles

Profiles in Figure 9 (right column) are segregated according to the mean data set value when convection is present for an average low-level RH (lowest 5 km, 76%). The average low-level RH for the samples collected above this data set mean value was 84%, while the value was 69% for the samples below the data set mean. Moist low-level moisture conditions (solid lines) are associated with increases in convective area fractions and in the ensemble mean mass flux profile. Vertical velocity weighted mean profiles do not give a clear indication whether updraft or downdraft mean velocities are enhanced under

Figure 11. As in Figures 7 and 9 but segregated according to traditional wet season (December to March, solid lines) and dry season (June to September, dashed lines) regime breakdowns.

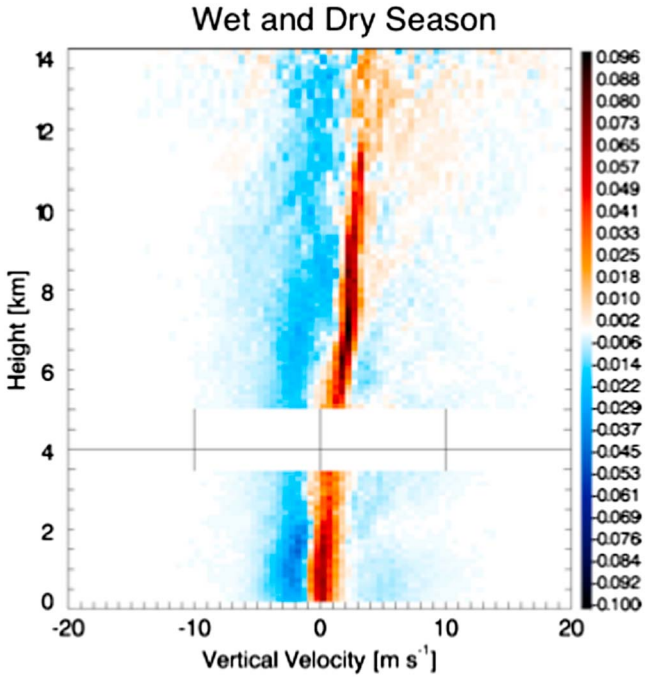

Figure 12. CFAD difference plot as in Figure 10 but for wet and dry season regimes. Red colors indicate more frequent wet season behaviors, whereas blue colors correspond to more frequent dry season observations.

moist/drier conditions, although a net upward motion seems favorable under moist conditions. However, the difference in CFADs constructed for low-level RH breakdowns (Figure 10, right) indicates that the drier conditions favor stronger and more diverse downdrafts, with some hints toward stronger updrafts, to deeper heights. The downdrafts and associated frequency are likely associated with the weak suggestions in Figure 9 for stronger downdraft mass flux profile behaviors under drier conditions to deeper heights. Overall, the mass flux profile properties in Figure 9 seem to be driven by differences in the updraft area fraction.

4.2.4. Wet and Dry Season Regime Breakdowns on Mass Flux Ensemble Mean Profiles

Since the annual cycles for several environmental quantities of interest discussed in previous sections are often coupled, it is prudent to explore profile breakdowns according to traditional Amazonian wet and dry season regimes (Figure 11). Wet season profiles during deeper convective events (solid lines) typically blend modest CAPE (mean ~ 1500 J kg^{-1} K^{-1}), weaker CIN (mean ~ −58 J kg^{-1} K^{-1}), and higher low-level moisture conditions (mean ~ 79%) between December and March. Dry season profiles (dashed lines) reflect when convection is present between June and September, conditions favoring higher CAPE (mean ~ 1900 J kg^{-1} K^{-1}), albeit reduced low-level moisture (mean ~ 70%) and stronger CIN (mean ~ −74 J kg^{-1} K^{-1}). From Figure 11, the most striking difference between the profiles is found with the substantially larger convective updraft area fraction under wet season conditions (Figure 11, middle). These differences translate to a factor of 2 increase for wet season average mass flux profiles (Figure 11, bottom). Dry season profiles reflect lower profile peak altitudes in area fraction and mass flux, which may indicate some increased relative contributions from cumulus congestus.

The CFAD difference between wet and dry season vertical velocity breakdowns is also provided in Figure 12. Dry season events illustrate broader velocity distributions, suggesting overall stronger velocities when convection is present. These observations are most reminiscent of CAPE breakdowns in Figure 10, intuitive since the dry season events are typically associated with higher CAPE magnitudes on days when convection is present. Wet season events show a much narrower distribution based on normalized frequency; however, they engulf the tails of the distribution that include the strongest vertical velocities observed for this data set (organized transitional events in March as in Figure 3, or following *Machado et al*. [2004]).

4.3. Relative Mass Flux Profile Breakdowns According To Echo Top Height

Approximately one third of the data set is associated with convective columns that register an ETH < 8 km. Since cloud frequency of occurrence in time and convective area fraction represents similar quantities, the mass flux profiles for "congestus" clouds defined based on simple ETH thresholds would be approximately half those from deeper convection, provided that the vertical velocity behaviors were similar. As from Figure 13, we find that mass flux profiles for these congestus (dashed lines) are roughly half the values found for deeper clouds (solid lines) at the heights where both sets of clouds are available. One interpretation is that mean congestus updrafts are not substantially weaker at these altitudes, perhaps in contrast to findings from *Schumacher et al*. [2015]. However, it is likely that simple ETH threshold methods may also be partially

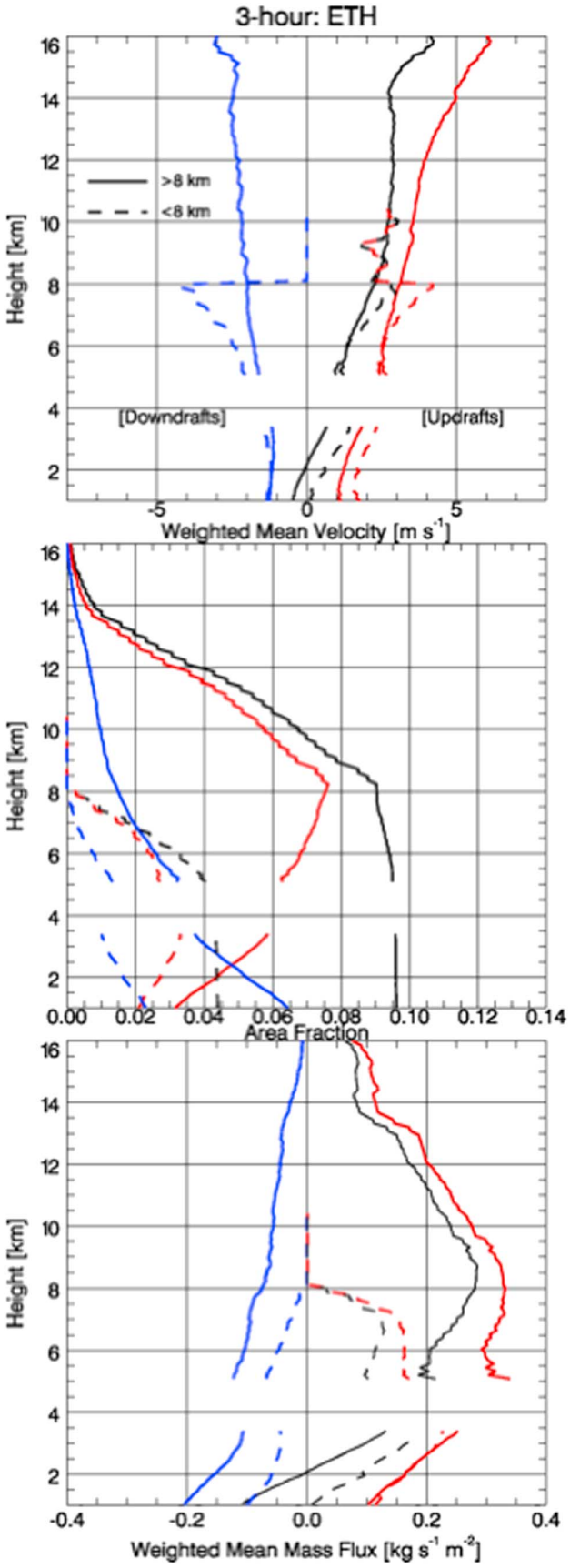

influenced by catching only the peripheries (chording) of deeper clouds, or not effective at isolating congestus from growing deep cumulus cloud behaviors. Unlike deeper convective clouds that indicate a substantial downdraft area fraction exceeding updraft fractions to lower altitudes, relative area fractions occupied by congestus downdrafts do not exceed that of updrafts to any altitude. This offers partial support that the chording of deeper clouds (those having developed convective downdrafts) is not a significant source of uncertainty.

5. Interpretation of Amazon Ensemble Profile Behaviors

The results from the previous sections align with many observations from the Darwin profiler studies performed by *Kumar et al.* [2015]. Although the Amazon convection indicates relatively smaller convective area fractions than those found from previous Darwin studies, the stronger mass flux profile magnitudes suggest that these smaller area fractions must be compensated by stronger vertical air motions for the Amazon storms (e.g., Figure 7). Nonetheless, the velocities are in line with previous Amazon expectations and weaker than typical for continental convective storms [e.g., *Anderson et al.*, 2005; *Giangrande et al.*, 2013], with 90th and 95th percentile values (Figure 8) typically not exceeding 10 m s^{-1}. Accordingly, these peak vertical velocities would typically not be sufficient to support significant storm electrification [e.g., *Zipser and Lutz*, 1994]. Interpretation and intercomparison with Darwin ensemble mean behaviors are challenging. One reason is because the previous Darwin study combined contributions from Active (widespread weaker convection) and Break (isolated, strong convection)

Figure 13. As in Figure 7 but breakdowns segregated according to echo top height values greater than 8 km (solid lines) and less than 8 km (dashed lines).

monsoonal regimes [e.g., *Pope et al*., 2009; *Giangrande et al*., 2014]. Consulting the subsequent Darwin scanning radar-based effort in *Kumar et al*. [2016], differences in estimated mass flux profiles between these regimes may be substantial (continental versus marine controls). Specifically, break monsoon regime storms associated with higher CAPE and CIN (having stronger vertical velocities) report reduced convective area fraction leading to overall lower average mass flux behaviors. Overall, these considerations highlight the importance for identifying the role of thermodynamic conditions or seasonal regime controls prior to aggregating, averaging, or interpreting ensemble mean profiles for model evaluation.

Nevertheless, thermodynamic and regime breakdowns add several important clues in line with previous Darwin efforts. Stronger CAPE suggests more intense vertical velocities, as directly viewed using CFAD difference fields (Figure 10, to approximately 10 km), or indirectly based reduced mean updraft fractions resulting in higher mean mass flux profiles (e.g., Figure 9). For downdrafts, the results are less pronounced; while velocities appear similarly enhanced and diverse according to CFAD differences, we observe only modest differences in mean downdraft area and downdraft mass flux profiles. Consulting CIN breakdowns, CIN values closer to zero when convection is present (Figure 9) are associated with additional mass flux peaked at higher altitudes, perhaps owing to additional convective activity and/or reduced frequency for shallower convective clouds reflected in these mean profiles. It should be noted that the stronger (more negative) CIN CFADs seem to also favor more diversity and stronger downdrafts to deeper altitudes (as with stronger CAPE). This result may seem counterintuitive; however, CAPE and CIN are independent parameters in these depictions. For the Amazon, relatively strong CIN is often associated with relatively stronger CAPE during the dry season—this dry regime may tend to inhibit weaker congestus "competition" [e.g., *Fu et al*., 1999; *Machado et al*., 2004] but begin to promote the deepest convective storms when evapotranspiration increases and added low-level moisture reduces CIN. Transitional months have already been previously identified as most active for storm electrification, and we also find these months associated with the highest updraft speeds [e.g., *Williams et al*., 2002; *Machado et al*., 2004; *Albrecht et al*., 2011]. This may offer partial explanation for some diversity in updraft and downdraft behaviors as attributed to our composite, isolated CIN and CAPE conditional breakdowns (e.g., transitional storms as those most associated with the strongest vertical motions above 10 km found in Figures 9 and 10).

Along with CAPE and CIN results, moist low-level RH conditions also favor higher convective area fraction and enhanced mass flux profiles when convection is present. However, downdraft mass flux profiles are relatively heightened under drier low-level RH conditions. This behavior was observed by *Kumar et al*. [2015] and interpreted as drier conditions compensating for less prolific convection by promoting, fewer stronger storms to deeper altitudes (enhanced entrainment also encouraging stronger downdrafts). Although we do not observe a dramatic preference toward stronger updrafts (transitional regimes perhaps favoring increasing moisture), CFADs in Figure 10 support arguments for stronger, more diverse downdrafts to higher altitudes that typically would accompany strong updrafts to those altitudes.

Moving to the traditional Amazon wet and dry season regime breakdowns (e.g., Figures 11 and 12) that couple regional scale CAPE, CIN and RH factors, the most pronounced discrepancies in observed ensemble profiles are driven by noticeable shifts in the convective area fraction. This may be interpreted as wet season months promoting more regular or larger coverage for convection, linked to seasonal changes that act to lower CIN. Interestingly, dry season events indicate the stronger, more diverse storm vertical velocities when convection is present (Figure 12). This may be interpreted that the average storm is potentially stronger when convection is present, e.g., higher average CAPE that also offsets stronger than average CIN. Higher CIN and lower low-level moisture could also be coupled in that conditions that promote fewer clouds and may promote more incoming solar radiation. This may also help promote larger land-surface contrasts such that the boundary layer air becomes more buoyant and contributing to stronger updrafts.

Additional attempts were also considered to segregate the GoAmazon2014/5 data set into ensemble mean profiles according to the upper and lower standard deviation values for CAPE, CIN, and low-level RH. One alternative was to explore basic correlations between the thermodynamic quantities of interest and velocity or mass flux profile values (as in other conventional GCM efforts) [e.g., *Suhas and Zhang*, 2015]. Unfortunately, those breakdowns typically reflected insufficient sample populations or required larger increments of the thermodynamic quantities (e.g., CAPE bins in 1000 J kg^{-1} K^{-1} increments) to generate representative profiles with confidence (peaked distributions as in Figure 4). Amazon wet and dry season regime multiparameter

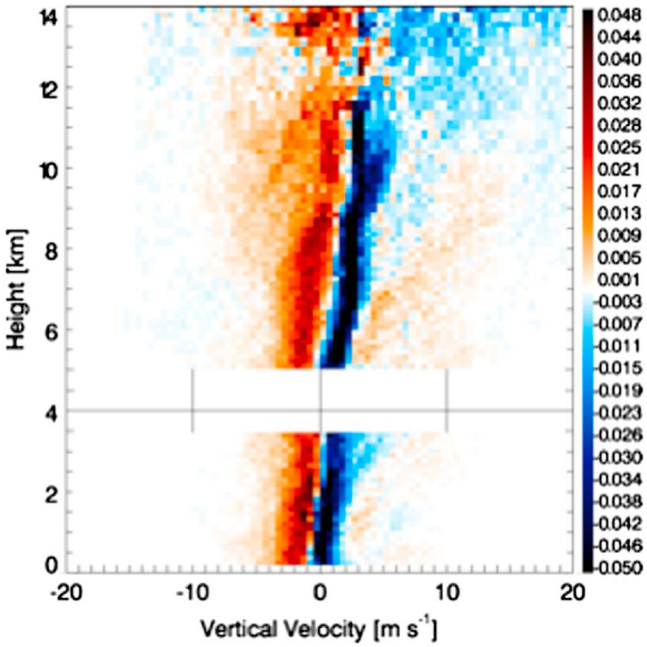

Figure 14. CFAD difference plot for CAPE as in Figure 10, now segregated according to the samples found one standard deviation above (stronger CAPE) and below (weaker CAPE) the data set mean. Deeper red colors indicate relatively more frequent observations during very strong CAPE conditions, whereas deeper blue colors correspond to more frequent observations during very weak CAPE conditions.

cross coupling also undermines the utility for those correlations. Sharper CAPE separations (e.g., upper standard deviation population, 3225 J kg^{-1} K^{-1}, minus lower, 485 J kg^{-1} K^{-1}; fewer than 100 samples in each) viewed in terms of vertical velocity CFAD differences (Figure 14) clearly demonstrate more pronounced enhancements than mean CFAD separations (Figure 10). Nevertheless, since the largest CAPE values are associated with Amazon dry season conditions having reduced low-level RH, one would also observe stronger velocity behaviors and correlations with reduced low-level RH. Overall, we recommended avoiding such correlation-based checks using RWP or similar observations until data collection to within wet or dry regime conditions could be better sampled.

Finally, it is important to discuss that the profile properties found in this manuscript reflect an ensemble domain convective condition that spans convective cloud lifecycle (initiation, mature, and decay phases). It is known that vertically pointing radars may miss, chord, and/or poorly capture any particular convective cell; however, average convective fractions and properties are suggested to be roughly similar over smaller to larger domains for Amazon convection. Previous profiling studies have proven that on longer-term ensemble averaging, chording of cylindrical convective cells implies that the statistical time-length (and therefore area coverage) for the clouds captured by profiling devices will be biased low (~22% undersampling) [e.g., *Jorgensen et al.*, 1985; *Borque et al.*, 2014]. This is unavoidable, but our comparisons between RWP temporal, point, and areal radar spatiotemporal scanning properties in section 2 suggest the RWP performs comparably to scanning radars that would not face this scrutiny. One fair criticism for chording, when coupled with additional beam filling issues to higher altitudes, is related to the likelihood the RWP will statistically sample the strongest peak vertical velocity magnitudes to within updraft cores with a correct frequency. Since we can be certain that the RWP will undersample and/or smear the centers of the convective cores (e.g., >1 km beam width at 10 km), it also follows that the RWP will undersample peak "subvolume" core magnitudes. Nevertheless, the underrepresentation of the strongest cores is a known sampling bias for other vertical velocity observations including aircraft measurements and multi-Doppler variational retrieval methods.

6. Summary

Our study makes use of an extended profiler data set from a 2 year Amazon basin deployment to help improve insights into convective vertical velocity, area fraction, and mass flux profiles. There is no one-size-fits-all solution toward improving GCM convective parameterization development. However, the observations of convective vertical velocity and mass flux over larger domains potentially offer one necessary constraint closer to the process level that GCM parameterizations are attempting to represent for evaluating mass flux-driven conventional GCM parameterizations and/or developing new GCM convective parameterizations [e.g., *Storer et al.*, 2015]. Our motivation is to present RWP column observations, when paired with justification from scanning radar data sets, in a manner suitable to multiple GCM convective parameterization audiences. Given the nature of the GoAmazon2014/5 data set, this necessitates emphasizing lengthier ensemble vertical velocity and mass flux profile depictions for determining whether models are providing

reasonable results and if those results vary with the larger-scale environment in a plausible manner. The overall findings on the vertical structure of convective mass flux, the relative role of convective area fraction and velocity on mass flux, and the sensitivity of mass flux profiles to changes in thermodynamic quantities of interest are consistent with previous profiler studies. A summary of the key findings is as follows:

1. Our results indicate qualitatively similar ensemble average mass flux profile behaviors and magnitudes to the previous results for ensemble mean tropical Darwin convective cloud studies at similar 3 h, 60 km-type spatiotemporal scales.
2. Updrafts and downdrafts are found to increase in magnitude with height to the midlevels (6–10 km, contingent on cloud top), consistent with all previous profiling and aircraft studies (updraft maximums to 20 m s^{-1}). The updraft mass flux also increases with height, while net mass flux profiles peak in magnitude and frequency above 8 km.
3. Downdrafts are the most frequent at low levels, and downdraft frequency generally decreases monotonically with height (with or without adjustments for fall speed behaviors).
4. Approximately one third of the convective area fraction we observe with the RWP is associated with cumulus congestus having ETH $<$ 8 km. For this data set, this also implied that congestus was associated with substantial mass flux for altitudes less than 8 km.
5. When considering various environmental controls when convection is present. stronger CAPE forcing conditions are associated with more intense vertical motions that lead to increases in mass flux profiles, despite lower convective area fraction. Segregating according to CIN controls, weaker CIN was associated with larger convective area fractions and increases in mass flux profiles. For low-level RH breakdowns, higher moisture conditions were associated with higher convective area fractions and higher net mass flux profiles.
6. Under traditional wet/dry season regime breakdowns, modest CAPE and low-level moisture with weakened CIN during the wet season tends to promote substantially higher area fraction leading to enhanced mass flux profile behaviors. The strongest storm vertical velocities for these data sets were observed during the transition months (e.g., March and October) that may not register as stronger CAPE based on the definitions in this study. Dry season storms when convection was present registered as substantially stronger than the typical convective storm observed during the wet season.

Acknowledgments

This manuscript has been authored by employees of Brookhaven Science Associates, LLC, under contract DE-AC02-98CH10886 with the U.S. Department of Energy (DOE). The publisher by accepting the manuscript for publication acknowledges that the United States Government retains a nonexclusive, paid-up, irrevocable, worldwide license to publish or reproduce the published form of this manuscript, or allow others to do so, for United States Government purposes. Zhe Feng at the Pacific Northwest National Laboratory (PNNL) and A. Protat at the Australian Bureau of Meteorology are supported by the U.S. DOE, as part of the Atmospheric System Research (ASR) Program. The PNNL is operated for DOE by Battelle Memorial Institute under contract DE-AC05-76RL01830. Funding was also obtained from the U.S. DOE, the São Paulo Research Foundation (FAPESP—2009/15235-8). The work was conducted under scientific licenses 001030/2012-4, 001262/2012-2, and 00254/2013-9 of the Brazilian National Council for Scientific and Technological Development (CNPq). Institutional support was provided by the Central Office of the Large-Scale Biosphere-Atmosphere Experiment in Amazonia (LBA), the National Institute of Amazonian Research (INPA), the National Institute for Space Research (INPE), Amazonas State University (UEA), and the Brazil Space Agency (AEB). We also acknowledge the Atmospheric Radiation Measurement (ARM) Climate Research Facility, a user facility of the U.S. DOE, Office of Science, sponsored by the Office of Biological and Environmental Research, and support from the ASR program of that office. All GoAmazon2014/5 data sets used in this study can be obtained from the ARM at http://www.arm.gov. The authors wish to thank GoAmazon2014/5 PI Scot Martin and the entire GoAmazon2014/5 ARM/AMF team (AMF Site Scientist, Mark Miller). Additional thanks to ARM mentor Richard Coulter for RWP data collection and maintenance and Vickal Kumar for helpful discussions on the Darwin data set. The authors also thank Aaron Funk (TAMU) for SIPAM remote data acquisition and radar-gridding preprocessing.

References

Albrecht, R. I., C. A. Morales, and M. A. F. Silva Dias (2011), Electrification of precipitating systems over the Amazon: Physical processes of thunderstorm development, *J. Geophys. Res.*, *116*, D08209, doi:10.1029/2010JD014756.

Anderson, N. F., C. A. Grainger, and J. L. Stith (2005), Characteristics of strong updrafts in precipitation systems over the central tropical Pacific Ocean and in the Amazon, *J. Appl. Meteorol.*, *44*, 731–738.

Arakawa, A., and W. H. Schubert (1974), Interaction of a cumulus cloud ensemble with the large-scale environment, Part I, *J. Atmos. Sci.*, *31*, 674–701.

Atmospheric Radiation Measurement (ARM) Climate Research Facility (2005), Updated yearly. W-Band (95 GHz) ARM Cloud Radar (WACR). 2014-03-01 to 2015-12-02, 3.21297 S 60.5981 W: ARM Mobile Facility (MAO) Manacapuru, Amazonas, Brazil; AMF1 (M1). Compiled by N. Bharadwaj, D. Nelson, B. Isom, J. Hardin, I. Lindenmaier, K. Johnson and A. Matthews. Atmospheric Radiation Measurement (ARM) Climate Research Facility Data Archive: Oak Ridge, Tenn. Data set accessed at. [Available at 10.5439/1025317.]

Atmospheric Radiation Measurement (ARM) Climate Research Facility (2006), Updated daily. Impact Disdrometer (DISDROMETER) 2011-04-27, 36.605 N 97.485 W: Southern Great Plains (SGP) Central Facility, Lamont, OK (C1). Compiled by M. Bartholomew. Atmospheric Radiation Measurement (ARM) Climate Research Facility Data Archive: Oak Ridge, Tenn. Data set accessed at. [Available at 10.5439/1025181.]

Atmospheric Radiation Measurement (ARM) Climate Research Facility (2009), Updated hourly, radar wind profiler (915RWPPRECIPMOM) Compiled by R. Coulter, T. Martin and P. Muradyan. Atmospheric Radiation Measurement (ARM) Climate Research Facility Data Archive: Oak Ridge, Tenn. Data set accessed at. [Available at 10.5439/1025128.]

Battan, L. J., and J. B. Theiss (1970), Measurement of vertical velocities in convective clouds by means of pulsed-Doppler radar, *J. Atmos. Sci.*, *27*, 293–298.

Berg, L. K., and R. B. Stull (2002), Accuracy of point and line measures of boundary layer cloud amount, *J. Appl. Meteorol.*, *41*, 640–650.

Borque, P., P. Kollias, and S. Giangrande (2014), First observations of tracking clouds using scanning ARM cloud radars, *J. Appl. Meteorol. Climatol.*, *53*, 2732–2746, doi:10.1175/JAMC-D-13-0182.1.

Burleyson, C. D., Z. Feng, S. M. Hagos, J. Fast, L. A. T. Machado, and S. T. Martin (2016), Spatial variability of the background diurnal cycle of deep convection around the GoAmazon2014/5 field campaign sites, *J. Appl. Meteorol. Climatol.*, *55*, 1579–1598, doi:10.1175/JAMC-D-15-0229.1.

Byers, H. R., and R. R. Braham (1948), The thunderstorm—Report of the thunderstorm project. U.S. Weather Bureau, Washington, D. C., June 1949. 287 pp.

Del Genio, A. D. (2012), Representing the sensitivity of convective cloud systems to tropospheric humidity in general circulation models, *Surv. Geophys.*, *33*, 637–656.

Del Genio, A. D., J. Wu, and Y. Chen (2012), Characteristics of mesoscale organization in WRF simulations of convection during TWP-ICE, *J. Clim.*, *25*, 5666–5688, doi:10.1175/JCLI-D-11-00422.1.

Donner, L. J. (1993), A cumulus parameterization including mass fluxes, vertical momentum dynamics, and mesoscale effects, *J. Atmos. Sci.*, *50*, 889–906.
Donner, L. J., C. J. Seman, R. S. Hemler, and S. Fan (2001), A cumulus parameterization including mass fluxes, convective vertical velocities, and mesoscale effects: Thermodynamic and hydrological aspects in a general circulation model, *J. Clim.*, *14*, 3444–3463.
Fabry, F., and I. Zawadzki (1995), Long-term radar observations of the melting layer of precipitation and their interpretation, *J. Atmos. Sci.*, *52*, 838–851.
Fu, R., and W. Li (2004), Influence of land surface on transition from dry to wet season over the Amazonia, *Theor. Appl. Climatol.*, *78*, 97–110.
Fu, R., B. Zhu, and R. Dickinson (1999), How do the atmosphere and land surface influence the seasonal changes of convection in tropical Amazon?, *J. Clim.*, *12*, 1306–1321.
Geerts, B., and Y. Dawei (2004), Classification and characterization of tropical precipitation based on high-resolution airborne vertical incidence radar. Part I: Classification, *J. Appl. Meteorol.*, *43*, 1554–1566.
Giangrande, S. E., E. P. Luke, and P. Kollias (2010), Automated retrievals of precipitation parameters using non-Rayleigh scattering at 95 GHz, *J. Atmos. Oceanic Technol.*, *27*, 1490–1503.
Giangrande, S. E., S. Collis, J. Straka, A. Protat, C. Williams, and S. Krueger (2013), A summary of convective-core vertical velocity properties using ARM UHF wind profilers in Oklahoma, *J. Appl. Meteorol. Climatol.*, *52*, 2278–2295.
Giangrande, S. E., M. J. Bartholomew, M. Pope, S. Collis, and M. P. Jensen (2014), A summary of precipitation characteristics from the 2006–11 northern Australian wet seasons as revealed by ARM disdrometer research facilities (Darwin, Australia), *J. Appl. Meteorol. Climatol.*, *53*, 1213–1231, doi:10.1175/JAMC-D-13-0222.1.
Giangrande, S., E. P. Luke, and P. Kollias (2012), Characterization of vertical velocity and drop size distribution parameters in widespread precipitation at ARM facilities, *J. Appl. Meteorol. Climatol.*, *51*, 380–391.
Hagos, S. M., Z. Feng, C. D. Burleyson, C. Zhao, M. N. Martini, and L. K. Berg (2016), Moist process biases in simulations of the Madden–Julian Oscillation episodes observed during the AMIE/DYNAMO field campaign, *J. Clim.*, *29*, 1091–1107.
Heymsfield, G. M., L. Tian, A. J. Heymsfield, L. Li, and S. Guimond (2010), Characteristics of deep tropical and subtropical convection from nadir-viewing high-altitude airborne Doppler radar, *J. Atmos. Sci.*, *67*, 285–308.
Hong, G. (2007), Radar backscattering properties of nonspherical ice crystals at 94 GHz, *J. Geophys. Res.*, *112*, D22203, doi:10.1029/2007JD008839.
Illingworth, A. J., et al. (2007), Cloudnet: Continuous evaluation of cloud profiles in seven operational models using ground-based observations, *Bull. Am. Meteorol. Soc.*, *88*, 883–898.
Jakob, C. (2010), Accelerating progress in global atmospheric model development through improved parameterizations: Challenges, opportunities, and strategies, *Bull. Am. Meteorol. Soc.*, *91*, 869–875.
Jensen, M. P., and A. D. Del Genio (2006), Factors limiting convective cloud top height at the ARM Nauru Island climate research facility, *J. Clim.*, *19*, 2105–2117.
Jensen, M. P., T. Toto, D. Troyan, P. Ciesielski, D. Holdridge, J. Kyrouac, J. Schatz, Y. Zhang, and S. Xie (2015), The MC3E sounding network: Operations, processing and analysis, *Atmos. Meas. Tech.*, *8*, 421–434, doi:10.5194/amt-8-1-2015.
Jensen, M. P., et al. (2016), The Midlatitude Continental Convective Clouds Experiment (MC3E), *Bull. Am. Meteorol. Soc.*, doi:10.1175/BAMS-D-14-00228.1, in press.
Jorgensen, D. P., E. J. Zipser, and M. A. LeMone (1985), Vertical motions in intense hurricanes, *J. Atmos. Sci.*, *42*, 839–856.
Kumar, V. V., C. Jakob, A. Protat, C. R. Williams, and P. T. May (2015), Mass-flux characteristics of tropical cumulus clouds from wind profiler observations at Darwin, Australia, *J. Atmos. Sci.*, *72*, 1837–1855.
Kumar, V., et al. (2016), The estimation of convective mass flux from radar reflectivities, *J. Appl. Meteorol. Climatol.*, *55*, 1239–1257, doi:10.1175/JAMC-D-15-0193.1.
Kumjian, M., S. Mishra, S. Giangrande, T. Toto, A. Ryzhkov, and A. Bansemer (2016), Polarimetric radar and aircraft observations of saggy bright bands during MC3E, *J. Geophys. Res. Atmos.*, *121*, 3584–3607, doi:10.1002/2015JD024446.
LeMone, M. A., and E. J. Zipser (1980), Cumulonimbus vertical velocity events in GATE. Part I: Diameter, intensity and mass flux, *J. Atmos. Sci.*, *37*, 2444–2457.
Lenschow, D. H. (1976), Estimating updraft velocity from an airplane response, *Mon. Weather Rev.*, *104*, 618–627.
Lerach, D. G., S. A. Rutledge, C. R. Williams, and R. Cifelli (2010), Vertical structure of convective systems during NAME 2004, *Mon. Weather Rev.*, *138*, 1695–1714.
Li, W., and R. Fu (2004), Transition of the large-scale atmospheric and land surface conditions from the dry to the wet season over Amazonia as diagnosed by the ECMWF Re-Analysis, *J. Clim.*, *17*, 2637–2651.
Machado, L. A. T., H. Laurent, N. Dessay, and I. Miranda (2004), Seasonal and diurnal variability of convection over the Amazonia: A comparison of different vegetation types and large scale forcing, *Theor. Appl. Climatol.*, *78*, 61–77, doi:10.1007/s00704-004-0044-9.
Martin, S. T., et al. (2015), Introduction: Observations and Modeling of the Green Ocean Amazon (GoAmazon2014/5), *Atmos. Chem. Phys. Discuss.*, *15*, 30,175–30,210, doi:10.5194/acpd-15-30175-2015.
Martin, S. T., et al. (2016), The Green Ocean Amazon Experiment (GoAmazon2014/5) Observes Pollution Affecting Gases, Aerosols, Clouds, and Rainfall over the Rain Forest, *Bull. Am. Meteorol. Soc.*, doi:10.1175/BAMS-D-15-00221.1.
Mather, J. H., and J. W. Voyles (2013), The ARM Climate Research Facility: A review of structure and capabilities, *Bull. Am. Meteorol. Soc.*, *94*, 377–392.
May, P. T., and D. K. Rajopadhyaya (1999), Vertical velocity characteristics of deep convection over Darwin, Australia, *Mon. Weather Rev.*, *127*, 1056–1071.
May, P. T., J. H. Mather, G. Vaughan, and C. Jakob (2008), Characterizing oceanic convective cloud systems—The tropical warm pool international cloud experiment, *Bull. Am. Meteorol. Soc.*, *154*, 153–155, doi:10.1175/BAMS-89-2-153.
Milbrandt, J. A., and M. K. Yau (2005), A multi-moment bulk microphysics parameterization. Part II: A proposed three-moment closure and scheme description, *J. Atmos. Sci.*, *62*, 3065–3081, doi:10.1175/JAS3535.1.
Miller, M. A., K. Nitschke, T. P. Ackerman, W. Ferrell, N. Hickmon, M. Ivey (2016), The Atmospheric Radiation Measurement Mobile Facility, *The Atmospheric Radiation Measurement (ARM) Program: AMS Monograph, The first 20 years of ARM*, Am. Meteorol. Soc., doi:10.1175/AMSMONOGRAPHS-D-15-0051.1.
Pope, M., C. Jakob, and M. J. Reeder (2009), Regimes of the north Australian wet season, *J. Clim.*, *22*, 6699–6715, doi:10.1175/2009JCLI3057.1.
Protat, A., and C. R. Williams (2011), The accuracy of radar estimates of ice terminal fall speed from vertically pointing Doppler radar measurements, *J. Appl. Meteorol. Climatol.*, *50*, 2120–2138.
Richter, I., and S. Xie (2008), On the origin of equatorial Atlantic biases in coupled general circulation models, *Clim. Dyn.*, *31*, 587.

Romatschke, U., and R. A. Houze Jr. (2010), Extreme summer convection in South America, *J. Clim.*, *23*, 3761–3791, doi:10.1175/2010JCLI3465.1.

Schumacher, C., S. N. Stevenson, and C. R. Williams (2015), Vertical motions of the tropical convective cloud spectrum over Darwin, Australia, *Q. J. R. Meteorol. Soc.*, *141*, 2277–2288, doi:10.1002/qj.2520.

Steiner, M. (1991), A new relationship between mean Doppler velocity and differential reflectivity, *J. Atmos. Oceanic Technol.*, *8*, 430–443.

Steiner, M., R. A. Houze Jr., and S. E. Yuter (1995), Climatological characterization of three-dimensional storm structure from operational radar and rain gauge data, *J. Appl. Meteorol.*, *34*, 1978–2007.

Stokes, G. M., and S. E. Schwartz (1994), The Atmospheric Radiation Measurement (ARM) Program: Programmatic background and design of the cloud and radiation test bed, *Bull. Am. Meteorol. Soc.*, *75*, 1201–1221.

Storer, R. L., B. M. Griffin, J. Höft, J. K. Weber, E. Raut, V. E. Larson, M. Wang, and P. J. Rasch (2015), Parameterizing deep convection using the assumed probability density function method, *Geosci. Model Dev.*, *8*, 1–19, doi:10.5194/gmdd-8-1-2015.

Suhas, E., and G. J. Zhang (2015), Evaluating convective parameterization closures using cloud-resolving model simulation of tropical deep convection, *J. Geophys. Res. Atmos.*, *120*, 1260–1277, doi:10.1002/2014JD022246.

Tokay, A., W. A. Petersen, P. Gatlin, and M. Wingo (2013), Comparison of raindrop size distribution measurements by collocated disdrometers, *J. Atmos. Oceanic Technol.*, *30*, 1672–1690.

Tridon, F., A. Battaglia, P. Kollias, E. Luke, and C. R. Williams (2013), Signal postprocessing and reflectivity calibration of the Atmospheric Radiation Measurement 915-MHz wind profilers, *J. Atmos. Oceanic Technol.*, *30*, 1038–1054.

Vila, D. A., L. Machado, H. Laurent, and I. Velasco (2008), Forecast and tracking the evolution of cloud clusters (ForTraCC) using satellite infrared imagery: Methodology and validation, *Weather Forecast.*, *23*, 233–245.

Wang, J., et al. (2016), Amazon boundary layer aerosol concentration sustained by vertical transport during rainfall, *Nature*, doi:10.1038/nature19819.

Williams, C. (2012), Vertical air motion retrieved from dual-frequency profiler observations, *J. Atmos. Oceanic Technol.*, *29*, 1471–1480.

Williams, E., et al. (2002), Contrasting convective regimes over the Amazon: Implications for cloud electrification, *J. Geophys. Res.*, *107*(D20), 8082, doi:10.1029/2001JD000380.

Xie, S., Y. Zhang, R. McCoy, M. P. Jensen, S. E. Giangrande, and M. Zhang (2015), Interactions between cumulus convection and its environment revealed by the MC3E sounding array, *J. Geophys. Res. Atmos.*, *119*, 11,784–11,808, doi:10.1002/2014JD022011.

Yin, L., R. Fu, E. Shevliakova, and R. Dickinson (2013), How well can CMIP5 simulate precipitation and its controlling processes over tropical South America?, *Clim. Dyn.*, *41*, 3127–3143.

Yuter, S. E., and R. A. Houze Jr. (1995), Three-dimensional kinematic and microphysical evolution of Florida cumulonimbus. Part II: Frequency distribution of vertical velocity, reflectivity, and differential reflectivity, *Mon. Weather Rev.*, *123*, 1941–1963.

Zipser, E. J., and K. Lutz (1994), The vertical profile of radar reflectivity of convective cells: A strong indicator of storm intensity and lightning probability, *Mon. Weather Rev.*, *122*, 1751–1759.

Zipser, E. J., and M. A. LeMone (1980), Cumulonimbus vertical velocity events in GATE. Part II: Synthesis and model core structure, *J. Atmos. Sci.*, *37*, 2458–2469.

Erratum

In the originally published version of this manuscript, the equation J kg^{-1} was erroneously published as J kg^{-1} K^{-1} for the measurements of CAPE and CIN. As a result, Figure 4 and Table 2 were published incorrectly. All corrections have been made to the online version of this article, but not the PDF, and the online version may be considered the authoritative version of record.

Table 2. The 2 Year GoAmazon2014/5 Data Set Frequency of Convective Occurrence for 3 h Average Properties, Separated According To Environmental and Regime Conditions

Condition	# of 3 h Samples	Subset < Mean > Values
CAPE > 1770 J kg^{-1}	217	2450 J kg^{-1}
CAPE < 1770 J kg^{-1}	197	1075 J kg^{-1}
CIN > −60 J kg^{-1}	245	−30 J kg^{-1}
CIN < −60 J kg^{-1}	169	−104 J kg^{-1}
RH [0–5 km] > 77%	237	84%
RH [0–5 km] < 77%	177	69%
Dry season, Jun–Sept	103	CAPE: 1900 J kg^{-1} CIN: −74 J kg^{-1} RH: 70%
Wet season, Dec–Mar	154	CAPE: 1500 J kg^{-1} CIN: −58 J kg^{-1} RH: 79%
Total, 3 h events	414	CAPE: 1768 J kg^{-1} CIN: −60 J kg^{-1} RH: 76%

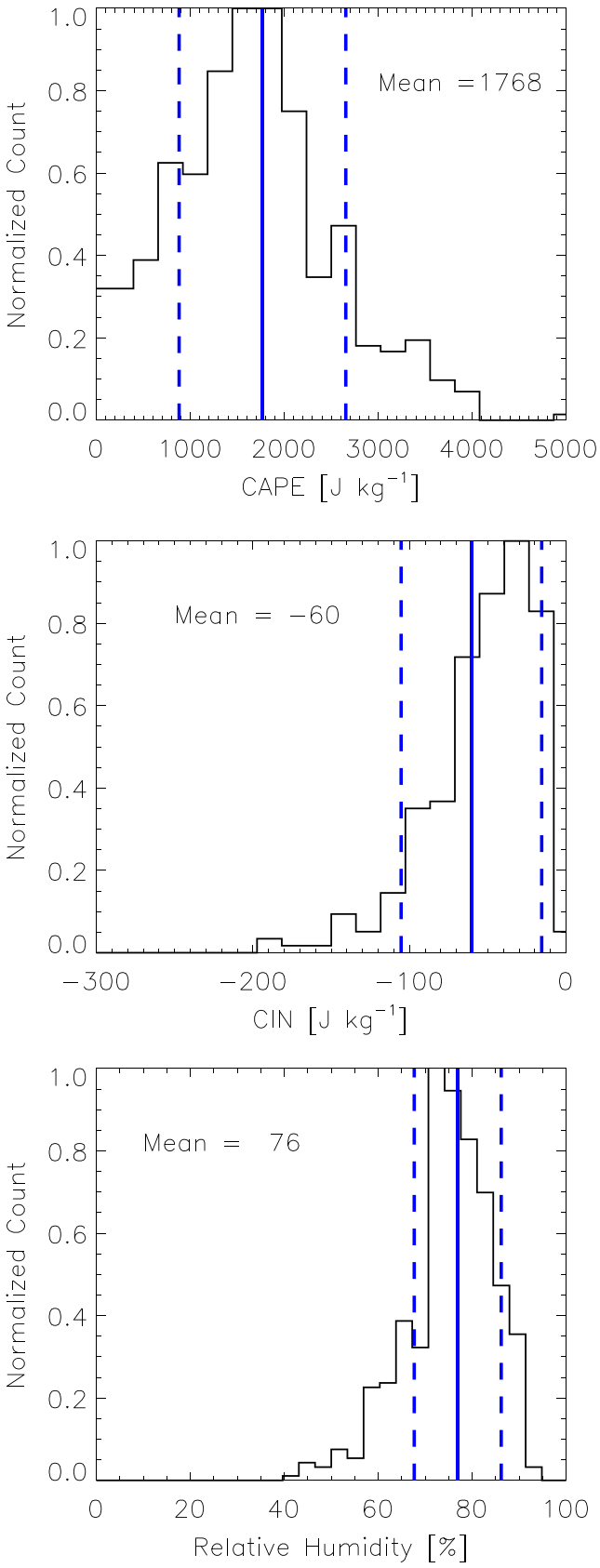

Figure 4. Frequency histograms for the surface-based CAPE, CIN, and low level (0–5 km) mean relative humidity RH (%) for event days in this study. Solid lines indicate the median values. Dashed lines indicate one standard deviation from the data set mean.